THESIS FOR THE DEGREE OF LICENTIATE OF ENGINEERING

Study of the flow-induced structure and anisotropy in lyotropic liquid crystals for hierarchical composites

ADRIAN RODRIGUEZ PALOMO

Department of Physics

CHALMERS UNIVERSITY OF TECHNOLOGY

Gothenburg, Sweden 2020

Study of the flow-induced structure and anisotropy in lyotropic liquid crystals for hierarchical composites
ADRIAN RODRIGUEZ PALOMO

Department of Physics
Chalmers University of Technology
SE-412 96 Gothenburg
Sweden
Telephone + 46 (0)31-772 1000

Printed by Chalmers Reproservice
Gothenburg, Sweden 2020

Study of the flow-induced anisotropy in lyotropic liquid crystals for hierarchical composites

Adrian Rodriguez Palomo
Department of Physics
Chalmers University of Technology

Abstract

Controlling the micro and nanostructure of materials is highly beneficial in order to tailor their physical properties. Extrusion-based 3D printing is a promising tool to produce hierarchical structures with controlled architecture. Combining additive manufacturing and self-assembled materials, complex structures with high anisotropy can be created. Lyotropic liquid crystals offer a wide variety of structures and compositions, in which hexagonal and lamellar phases are very interesting options. Far from the idealistic concepts of 3D printing and extrusion, the variability of the different systems, physical properties of the inks and environmental conditions play a fundamental role in the appearance of imperfections, undesired nanostructures and the limitation in the maximum effective alignment achieved.

To understand the mechanisms that induce alignment in liquid crystalline phases and produce secondary effects and imperfections, a combination of different methods was utilized. Using small angle X-ray scattering as the main characterization tool, the nanostructure of the liquid crystals as well as the anisotropy was measured. The use of imaging techniques adds an extra dimension which brings a broader view of the self-assembled structure. Microfluidic channels were used to study the mechanisms of alignment in the confined space offered by the nozzle walls and the high pressures applied in the printing process. The confined flow in the printing nozzle has different properties and constrains compared to the open flow that the extruded filament encounters in the printing platform, which was studied by *in-situ* 3D printing in the X-ray beam. By complementary rheological characterization, a more detailed analysis understanding of the flow behaviour was achieved and birefringence microscopy opened up the possibilities of a time resolved study of the anisotropy in the filament.

The results demonstrated the role of the shear stress in liquid crystals in confined flow, highlighting both the effect it has on the anisotropy as well as on morphological transitions in the self-assembled structures. The performed experiments also reflect on the possible causes of misalignment such as stress release and try to find the optimal parameters in the nozzle design which lead to the best alignment in terms of homogeneity in the strand and maximizing the orientation. Finally, the results also show the importance of time and environmental conditions during 3D printing, which may affect the final structure and orientation prior the fixation of the nanostructure.

Keywords: Self-assembly, Lyotropic liquid crystals, 3D printing, SAXS, Birefringence microscopy, Microfluidics, Rheology, Hierarchical materials.

List of Papers

This thesis is based on the following papers:

I *In situ* visualization of the structural evolution and alignment of lyotropic liquid crystals in confined flow.
A. Rodriguez-Palomo, V. Lutz-Bueno, X. Cao, R. Kádár, M. Andersson, M. Liebi.
Submitted

II Nanostructure and anisotropy of 3D printed lyotropic liquid crystals studied by scattering and birefringence imaging.
A. Rodriguez-Palomo, V. Lutz-Bueno, M. Guizar-Sicairos, R. Kádár, M. Andersson, M. Liebi.
Manuscript.

Contribution Report

I M.L. and M.A. designed the project. A.R. prepared the samples and performed the experiments with the assistance and support of X.C in the microfluidics production, V.L. in X-ray experiments and R.K. in the rheology characterization. The data was analysed by A.R. with the assistance of M.L. regarding the scattering and R.K. the rheology experiments. A.R. prepared the manuscript and all the authors discussed the results and reviewed the manuscript. All authors have given approval to the final version of the manuscript.

II A.R. and M.L. designed the idea of the experiment. A.R. did the sample preparation and performed the scattering experiments together with M.L, assisted by V.L. The birefringence imaging was carried out by A.R. as well as the rheology characterization, which was assisted by R.K. The data was analysed by A.R. with the assistance of M.L. regarding the scattering and R.K. the rheology experiments. A.R. prepared the manuscript and all the authors discussed the results and reviewed the manuscript. All authors have given approval to the final version of the manuscript.

Table of Contents

Abstract ..... *III*

List of Papers ..... *IV*

Contribution Report ..... *V*

Table of Contents ..... *VII*

Chapter 1 - Introduction **1**

Chapter 2 - Self-assembled hierarchical materials **3**

2.1. Materials in the nanoscale and self-assembly *3*

2.2. Liquid crystals *5*

2.3. Hierarchical structures *6*

2.4. Inducing anisotropy *8*

Chapter 3 - Materials and Methods **11**

3.1. Sample Preparation *11*

3.2. Microfluidics Preparation *12*

3.3. Small Angle X-ray Scattering (SAXS) *14*

3.3.1. Scanning SAXS *17*

3.4. Rheology *18*

3.5. Birefringence Microscopy *19*

Chapter 4 - Results and Discussion **21**

4.1. Self-assembled structure of lyotropic liquid crystals *21*

4.1.1. Small Angle X-ray Scattering *21*

4.1.2. Rheological characterization *23*

4.2. Confined flow and anisotropy *25*

4.2.1. Influence of the flow rate and channel design *25*

4.2.2. Morphological changes during flow *27*

4.3. In situ 3D printing and study of the induced anisotropy *29*

4.4. Phase transformations, relaxation and evolution of the alignment *30*

Chapter 5 - Conclusions and Outlook **35**

Acknowledgements **37**

Bibliography **39**

Chapter 1

Introduction

Human history has been supported by the use of natural materials such as wood, bone or stone to create tools and structures that allowed a better life quality. The transition from natural to synthetic materials was driven by the necessity of an improved performance over a longer period of time, with stronger, lighter and tougher materials at a lower cost and with the possibility of mass production. However, the current economic growth and expansion rates of modern societies require materials that can overcome the challenges of transportation, medicine or energy production. Synthetic materials as they have been used in the last century are becoming obsolete, highly inefficient and unsustainable. It is now time to make a better use of the available resources and use materials smarter. Natural materials are catching the attention of scientists and engineers again for their unique and complex structures in a smaller length scale. Inspired by the hierarchical architecture of natural materials, a new research branch in functional and structural materials is being directed towards bioinspired and biomimetic structures. However, mimicking the structures of natural materials is not a trivial issue. Natural materials are typically made of a very limited number of components available in the surroundings of the environment, with usually poor intrinsic properties. Years of evolution and adaptation assembled them in complex structures with features in the nano, micro and macroscale. The new characterization tools, able to reach from millimetres to subatomic resolution allow us to decipher such intricated architectures.[1]

Centred in the current needs of modern medicine, the field of biomaterials is rapidly expanding. The target in this field has been to replace defective or damaged tissue with synthetic bulk materials, which were designed to avoid any interaction and go unnoticed by the organism. More recent strategies imitating natural structures aim to produce materials with high performance which can also interact with the biological environment and be part of the organism. Examples of this can be found in the use of scaffolds for bone regeneration. In contrast with the old ceramic fillings and metallic structural parts for bone replacement, composite scaffolds that can integrate in the defect and promote the growth of new bone are the target of scientists and medical doctors. The scaffolds do not aim to offer mechanical support or be a permanent substitute of the missing part, but serve as a matrix where the original tissue can quickly grow and recover its functionality. This is achieved by imitating the natural environment, artificially creating the appropriate environment for cells to populate and divide.[2] In an optimal case, the scaffold will eventually dissolve without a trace of any synthetic material, leaving the native tissue.

Often, not only structural support is wanted but recovering the functionality of an organ is desired. Analogous to that strategy, soft tissue is also created by a (often polymeric) scaffold or template mimicking the original collagen matrix or fibrillar tissue. To form functional biomedical devices and scaffolds, materials compatible with the aqueous environment of the body, that are non-toxic and capable to interact with the environment without causing rejection or foreign body reactions are needed. Examples of a smart use of materials forming hierarchical structures inspired by nature are the self-assembled structures. Inducing anisotropy in the nanoscale makes it possible to create materials with anisotropic physical properties. These materials can be used e.g. for hearth valve replacements, where a fibrinous flexible tissue with anisotropic mechanical properties is needed.[3]

The starting point of this project was the biomimetic composites inspired by the bone-cartilage interphase previously developed.[4] Mimicking the structure of collagen fibres and hydroxyapatite nanoplatelets in bone, it consists of aligned self-assembled lyotropic liquid crystals, which are crosslinked and mineralised with calcium phosphate nanoparticles. To control the long-range anisotropy, the composites are fabricated into hierarchical structures using extrusion-based 3D printing as manufacturing method. The self-assembled polymeric matrix is printed and crosslinked to be mineralised in a further step. To reach a complete control of the induced anisotropy, a more detailed and systematic study of the 3D printing process is necessary. The goal of the work presented in this thesis was to investigate and understand the processes that lead to alignment of self-assembled lyotropic liquid crystals pursuing the final application as 3D printed hierarchical materials.

This work is divided in two main sections: The confined flow inside the nozzle, which induces the alignment, and the open flow during the extrusion of the filament in the printing platform. Small angle X-ray scattering complemented with birefringence microscopy were used to study the anisotropy as well as rheological measurements to understand the different steps that the liquid crystals were subjected to during the flow in the 3D printing. This work aimed to establish a systematic method to study the flow properties and processes that are directly involved in the alignment of liquid crystals during 3D printing, which could be further expanded to other similar materials.

Chapter 2

Self-assembled hierarchical materials

This chapter is focused on the impact of nanomaterials in materials science and in self-assembly as a basic process in the creation of hierarchical structures. The theory is centred around the use of macromolecules as the building blocks such as the amphiphilic co-polymers employed in the development of this thesis. A literature review of the most important work related with synthetic hierarchical materials is included that set the ground for this and other studies about complex hierarchical structures.

2.1. Materials in the nanoscale and self-assembly

In the last decades, the interest in materials with controlled structures in the nanoscale has increased enormously due to the development of new production and characterization methods that brought a whole new world to science.[5,6] The big impact of these methods comes from the interest on manipulating atom-by-atom (equivalent to molecule-by-molecule) to create new structures at the nanoscale.[7] New devices were possible with improved performances and functionalities than the ones fabricated by the standard manufacturing technologies. Gas and biosensors have widely been investigated by the use of the high specific surface and plasmonic properties of nanoparticles.[8] The field of electronics, optoelectronics and photovoltaics was greatly benefitted by the use of nanomaterials such as thin films, nanoparticles, nanotubes and nanowires.[9] In biomedicine, numerous improvements have been made thanks to the access and development of nanomaterials compatible with the organism that reduce the drug usage, smartly target cancer cells or allow us to track and treat complex diseases.[10,11] There are two general routes for the formation of nanomaterials known as *top-down* and *bottom-up*. The *top-down* strategy has been used mainly in physics and engineering and consists of reducing the dimensions of a macroscopic material via mechanical, chemical or optical processes. The efficiency of this method is considerably low, and the maximum resolution is limited by the techniques (usually around 100 nm). In contrast to this approach, in the *bottom-up* route basic units such as atoms or molecules are hierarchically assembled in larger structures via chemical or physical processes. The size of the materials created is in the range of nanometres however, the production of those materials is driven by chemical and/or physical forces which are sometimes hard to control and predict. A combination of both approaches is also often used, where *top-down* and *bottom-up* routes achieve the best results for a specific application.[12]

Certain macromolecules such as block co-polymers, are used as a molecular unit in *bottom-up* synthesis of nanomaterials. These types of polymers offer a very well controlled structure and composition of repeated organic molecules that form the different blocks which are covalently linked together in long polymer chains. They are composed of two or more segments with different chemical composition and often contain hydrophilic and hydrophobic blocks which give them an amphiphilic behaviour. The interests of these block co-polymers lie in their ability to self-assemble in organized structures. Self-assembly is a process where individual components organise in larger ordered structures by the action of local interactions without any external forces. The building blocks in self-assembled structures can vary from molecules to macromolecules, particles and aggregates. Self-assembly is a common feature in biology, where biomolecules and phospholipids organise forming the cell membranes that compose every living entity.[13] The driving force for the self-assembly of amphiphilic macromolecules is the minimization of the free energy, dominated by weak Van der Waals forces, hydrogen bonds and electrostatic interaction. This is translated in an interaction between the hydrophilicity / hydrophobicity of each block in a given environment.[14] In a polar solvent, the hydrophobic block tends to stay away from the solvent, giving as a result the association of several co-polymer chains together so that the hydrophilic block(s) face the polar domain and the hydrophobic block(s) form what is now the apolar domain (see Figure 2.1) in what is called the micellization process in solutions or the microphase segregation in concentrated systems.[15, 16] This process reduces the total free energy of the system when the hydrophobic chains dissociate themselves from the polar environment. In the case of the systems described within this thesis, an association of polymeric chains need to occur and ordered clusters of polymer chains are formed with different geometries defined by the total concentration of polymer in the system.[17] This process can be enhanced by adding an apolar solvent to the mixture. The presence of an apolar solvent in a polar environment facilitate the creation of polar/apolar domains as well as the assembly of polymer chains in their interphase.

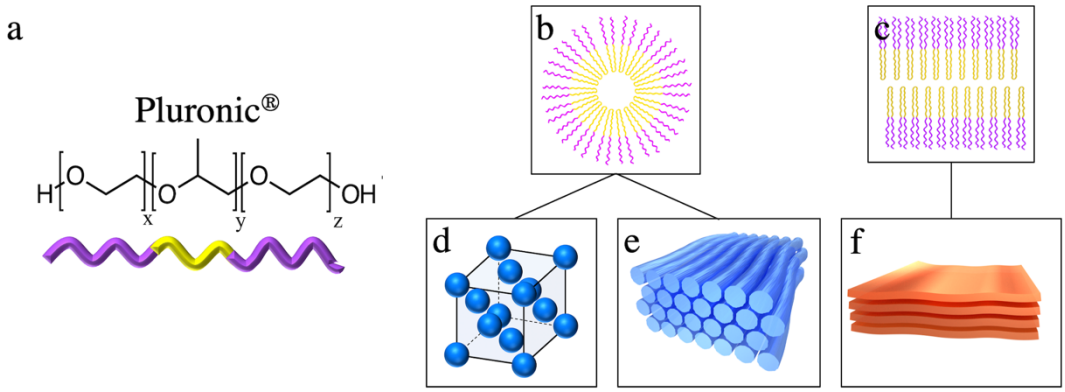

Figure 2.1. Formation of self-assembled structures in block co-polymer systems. The amphiphilic block copolymer used in this thesis (a), Pluronic®, is assembled in spheres (d), cylinders (e) or bilayers (c, f) which can get an extended range of order in the microscale.

Depending on the chemical composition and amphiphilic structure, an extensive variety of arrangements can be achieved. Dominated by the packing parameter, the final shape of the self-assembled structure is defined by the volume and contact area of the polar and apolar chains of the polymer in the different conformations of the hydrocarbon chain. Spheres, cylinders, worm-like micelles (cylinders with micrometre length), vesicles and bilayers are some of the possible structures among many other.[18, 19] The basic parameters which control the assembly of these structures in the case of block co-polymers are defined by the block composition (i.e. ratio of hydrophilic/hydrophobic blocks and their length), concentration, temperature, solvent, pH, etc. The action radius of self-assembly does not end in the molecular scale, and such systems are able to re-arrange in nanoscale forming complex superlattices under certain conditions.[20, 21]

2.2. Liquid crystals

Unlike other crystalline materials, which are associated with a solid and stiff behaviour, liquid-crystalline materials have a liquid-like fluidity and an anisotropic arrangement of their molecular components. They can be described as materials with a degree of order between the complete disorder of a liquid and the three-dimensional long-range order of a crystal.[13] They have what is called orientational order and may also have a positional order.[22] This order distinguishes them from regular liquids from a structural point of view and from their anisotropic physical properties. Molecular anisotropy is the key to liquid crystals, which are usually formed by stiff molecules with high aspect ratio either length-to-diameter (needle-like) or diameter-to-thickness (discs). The existence of a liquid-crystalline state is often guided by the interaction between molecules and the volume constrains imposed by a highly concentrated and densely packed system. An illustrative example is thermotropic liquid crystals, which transit between the ordered and disordered state by changes in their temperature. Reducing the temperature of the system, molecules do not have enough available energy to overcome the intramolecular rotational-energy barrier and they adopt more extended conformations. This leads to an increase in the volume of the molecule and therefore in the molecular interaction energy that is minimized by acquiring a more densely packed fraction and increased long-range order. On the other hand, in so-called lyotropic liquid crystals, a transition to an ordered state can also be produced by a change in concentration. Whereas thermotropic liquid crystals do not need solvent to form liquid crystal phases, lyotropic liquid crystals are always formed by amphiphiles in solution. Their crystalline structure is defined by the concentration of polymer, i.e. by increasing the concentration of molecular units the available free space is reduced and a liquid-crystalline order is favored.[22]

The liquid crystalline state is generally discussed with simple molecules; however, the production of those materials is not only limited to molecules, but some other larger structures have been proven to form liquid crystals. Rod-like inorganic particles have been observed forming liquid crystalline phases[23] as well as long peptide molecules assembled in fibres forming lyotropic liquid crystals.[24] Block co-polymers in water or a solvent mixture represent

one category which form lyotropic liquid crystals. The phase diagrams of the lyotropic liquid crystals used within this thesis is introduced in Section 3.1. Block co-polymers, self-assembled in micelles, cylinders, bilayers, etc, become suitable building blocks to create liquid crystals. The interaction and assembly of these larger structures create a new level of hierarchy in a larger length-scale. A hierarchical structure with two different types of long-range order is thus formed: in the molecular and in the aggregate scale.[25] The nanostructures created by self-assembled processes can be used in the *bottom-up* approach as ordering mechanism at the lower length scales. In order to create hierarchical systems, the control over the macro and microstructure is crucial as well and it is elaborated in the following two sections.

2.3. Hierarchical structures

Hierarchical structure corresponds to an arrangement of items in a structured organization with different levels of importance or ordered at different levels. In natural sciences and engineering, hierarchical materials are associated with structures in which there is an organization in different sublevels, each of them composed by different subunits. Each of these subunits form the building blocks for the next level and may have different physical and/or chemical properties than the units of the levels above or below. Thus, hierarchical materials need to fulfil two requirements. First, its building blocks have to be present in more than one length scale, and second, the properties of the different structural units have to be different but have complementary functionality. This can be fulfilled by creating an arrangement of subunits of either the same material but different dimensions or units of different materials in a composite.[26]

Hierarchical materials are widely found in nature,[27] from dendritic mineral growth, structural support in biology or unique abilities and functionalities in plants and animals. These hierarchical materials are often created by self-assembly mechanisms perfectioned during thousands of years of evolution and adaptation to the environment. One fascinating example is the adhesion exhibited by geckos on rough surfaces without the use of any secretion or adhesive. As illustrated in Figure 2.2 panel a, the pads of geckos are composed of several structures which contains thousands of hair-like structures called *setae*. Each *seta* is also composed of hundreds of fibrillar endings called *spatulae* which multiply the active surface area in contact with the walking surface, adapting to its roughness. The adhesion is due to Van der Waals interactions created by thousands of nanoscopic fibres on the surface. This types of structures are being used by researchers and engineers to inspire new materials with exceptional functionalities.[28] Another example of hierarchical materials created by nature, this time using multi-material composites, is bone. In bone, collagen molecules form long fibres which are assembled in bunches with intercalated ceramic hydroxyapatite nanoplatelets. Several of those bunches of fibres oriented in the same direction create collagen fibrils which are packed in geometrical structures with very defined orientation such as lamellae and osteons. Those structures create the cortical (compact) and trabecular (spongy)

bone, creating a polymer-ceramic composite with high anisotropy that forms the skeleton of vertebrates.[1]

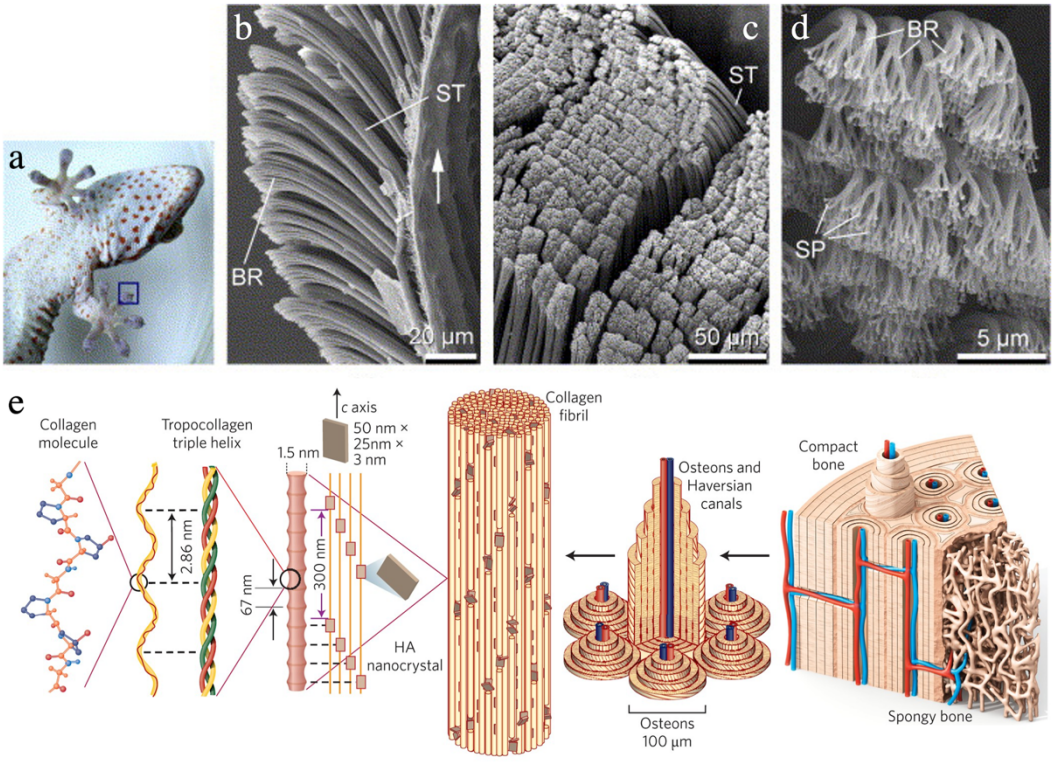

Figure 2.2. Hierarchical structure of gecko pads at different magnifications (a-d). The surface of the pads is covered with hundreds of microscopic *setae* (ST), which have hundreds of *spatulae* (SP). Hierarchical structure of cortical bone (e). Compact bone is composed of osteons, which have a lamellar structure. Each individual lamella consists of an arrangement of fibres made of several mineralised collagen fibrils. Fibrils are made of collagen protein molecules composed by three chains of amino acids and hydroxyapatite nanoplatelets. Adapted with permission from Gao et al.[29] (Copyright 2005, Elsevier) and Wegst et al.[1] (Copyright 2015, Nature Publishing Group).

Focusing on these two examples, many strategies have been developed to mimic the hierarchical structures, synthetising new materials using both *top-down* and *bottom-up* approaches. Adhesive surfaces bio-inspired from gecko pads have been created using photolithography as a *top-down* method to carve the surface of the material with specific patterns and/or *bottom-up* methods such as templating, where a scaffolds or template is used to steer the growth of nanofibers or other nanostructures. The combination of several steps of material processing can create surfaces with multiple small flat structures similar to the gecko *setae* covered with nanometric fibres that achieve high adhesion rates.[30, 31] Templating is a very common method to produce bone-mimetic composited as well. As a general approach, fibrillar structures are used as a template for a further mineralization step. Calcium phosphate solutions are often infiltrated in the fibrillar matrix, where amorphous ceramic particles precipitate in the gaps. When aged, amorphous calcium phosphate transforms into crystalline hydroxyapatite, which is the most common ceramic component in bone. This method is inspired by the natural growth of bone tissue, following the original mineralization process of collagen fibres.[32] As discussed above, bone has a highly anisotropic nanostructure, which

define its mechanical properties. The use of self-assembly to create the polymeric matrix before the mineralization step is of high interest since it can define the structural anisotropy at the nanoscale. Liquid crystals of block co-polymers can be used for this purpose, in which hexagonally packed cylinders are acting as the collagen fibres. Bilayers can be used in a lamellar stack as in the lamellar compact bone. When mineralised, the ceramic particles also have a high anisotropy, which confers them different mechanical properties in the different directions of load.[4]

2.4. Inducing anisotropy

The anisotropy in the nanoscale can be extended to the micro and macroscale using different processing methods such as additive manufacturing. Most commonly known as 3D printing, additive manufacturing is a production method in which objects are manufactured from a CAD (Computer-Aided Design) model layer-by-layer. Slicing the total volume of the object in thin layers allows to produce geometries with high complexity avoiding the use of moulds, dies and generating much less or no excess waist material. This method has raised a high academic and industrial interest in the recent years, which led to the development of multiple technologies for every type of materials and environments.[33] Among all the different technologies, extrusion-based 3D printing is of high interest for anisotropic materials. The printing material (i.e. the ink) in a fluid-like state is loaded in a cartridge and extruded through a nozzle which produces a continuous filament. A mobile platform in the horizontal plane (xy-plane) produced the layer geometry and a stage in the z-axis allows to move between layers.

The interest in this method lies in the effect that extrusion has on the ink containing particles or molecules with shape anisotropy as explained in Figure 2.3. Anisotropic filaments are of high interest in science and technology as for example for the production of 3D printed optically responsive devices[34] or the creation of composites with complex hierarchical structures[35]. The nozzle is designed with a constriction towards the outlet that reduces the inner space, increasing the velocity of the fluid in that point. The generated extensional flow in the central part creates a stretching strain in the ink, which may eventually align the anisotropic molecules, polymeric chains or particles in the flow direction. The small dimensions of the nozzle also generate high shear rates in the proximities of the walls, which also contribute in the alignment process. During shear, fluids with anisotropic component tend to align in the shear plane, reducing the interparticle interaction, which reduces the viscosity and facilitates the flow in what is known as shear thinning. The variability in the nanostructure and rheology of the different printing materials brings about the importance to evaluate the behaviour and effect of extensional and shear forces in each system.

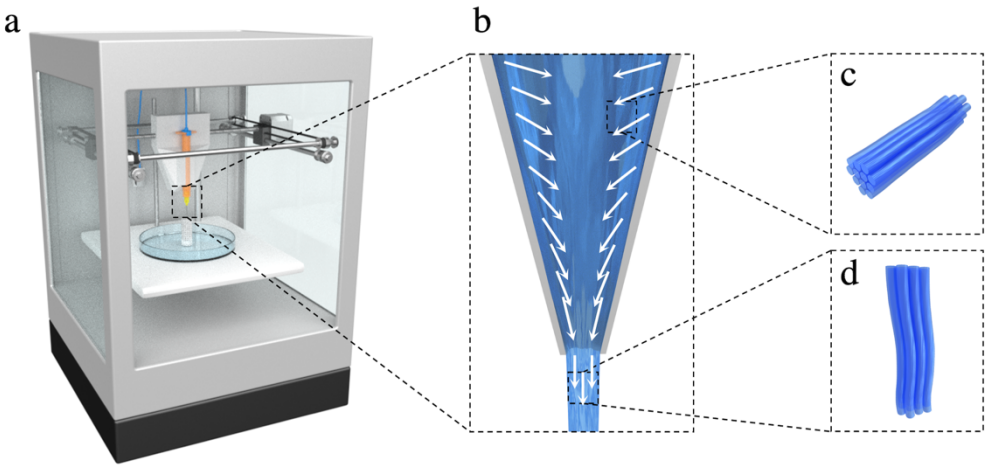

Figure 2.3. 3D printing can be used to induce macroscopy anisotropy in hierarchical materials. The fluid in a cartridge is 3D printed by extrusion (a), which aligns the entitles that form the liquid crystals. The flow in the 3D printing nozzle (b) induce alignment by extensional and shear flows. The white arrows indicate the most common/probable directions of flow, where the nano entities of the liquid crystal are expected to be found oriented (c-d).

There are multiple methods to analyse the anisotropy in the nanoscale, where several fields use different calculations adapted to the different measuring techniques. High resolution microscopy techniques (e.g. scanning and/or transmission electron microscopy, etc.) are able to directly visualize the structures. They rely on image analysis algorithms which identify shape, size and other contrast parameters; however, they only reach a small field of view and achieving a complete overview is sometimes difficult. Methods to indirectly probe the alignment of the material include techniques such as scattering or birefringence (see Chapter 3 for more details). They use the interactions of photons with matter to probe the nanostructure of materials, which lead to an anisotropic scattering, diffraction of refraction.[36]

Several approaches have been developed to estimate or quantify the degree of mutual alignment of nanoelements, or in more general words, how much (or how less) randomness is in the observed material. Taking a bunch of fibres as a model, one extreme case would be when all of them are distributed perfectly isotropic and the average orientation is therefore 0. No preferential direction is observed. The other extreme case would be when the fibres are perfectly aligned in a given direction, the averaged orientation of the system is the direction of any of the fibres and the standard deviation is 0. In this frame, any possibility in between both extremes will contain certain amount of order and certain amount of disorder/randomness which is attempted to be quantified by the orientational order parameter. The orientational order parameter S_N (Equation 2.1) describes the distribution of orientations of the anisotropic axis of molecules, particles or fibres, where a perfectly aligned system will result in a value of 1, a perfectly disorder system in a value of 0, and -0.5 in case of perpendicular alignment.

$$S_N = \frac{3\langle \cos^2 \theta \rangle - 1}{2} \qquad \text{Equation 2.1}$$

The orientational distribution function $P(\theta, \phi)$ in spherical coordinates, with the polar (θ) and azimuthal (ϕ) angles, relates with the orientational parameter through Equation 2.2.[22] This method is extendedly used in the Hermans' Orientation Parameter in scattering (described in Section 3.3) or in birefringence experiments, applied to materials with a high degree of anisotropy.

$$\langle \cos^2 \theta \rangle = \frac{\int_0^{\pi} \int_0^{2\pi} \cos^2 \theta \, P(\theta, \phi) \sin \theta \, d\phi \, d\theta}{\int_0^{\pi} \int_0^{2\pi} P(\theta, \phi) \sin \theta \, d\phi \, d\theta} \qquad \text{Equation 2.2}$$

Chapter 3

Materials and Methods

The following chapter describes the procedures during the sample preparation and the characterization techniques used in the performance of all the experiments included in this thesis. The basic theory behind the methods as well as the essential equations used for the data analysis are explained with the aim of setting the basic scientific background to understand the results presented in Chapter 4. The measurement parameters and other details are not included in this chapter but can be found in the methods section of the appended papers at the end of this thesis.

3.1. Sample Preparation

The lyotropic liquid crystals were prepared dissolving the block co-polymer in water or in a mixture of water and a water-immiscible solvent. In the appropriate ratio, the minority solvent creates micro or nano droplets where the polymer is located at the interface. The hydrophilic block is dissolved in the polar liquid, while the hydrophobic block locates in the apolar solvent creating the different self-assembled structures guided by the interfaces of the two liquid phases. In the absence of apolar solvent, micro segregation takes place. The hydrophilic block is dissolved in water while the hydrophobic parts interact with each other to form isolated apolar domains. In both cases, a vigorous mixing is necessary to facilitate the creation of the polar/apolar interface and to homogenise the mixture since the concentration of polymer and solvent will define the self-assembled structure.

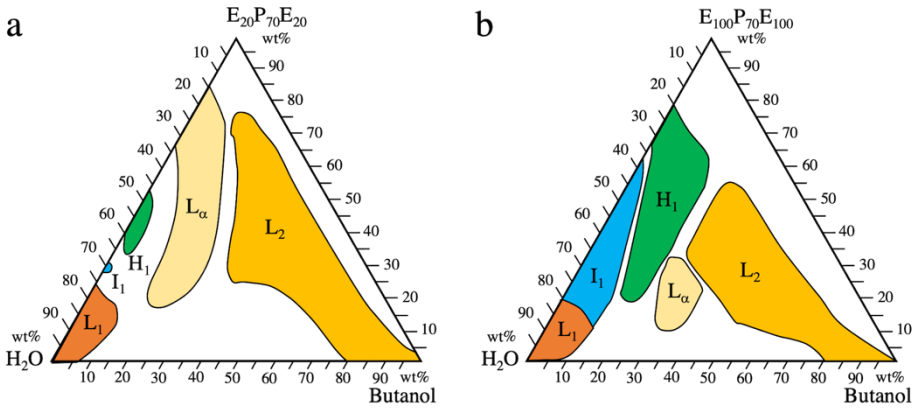

Figure 3.1. Phase diagrams of the ternary system Pluronic®-Water-Butanol for the polymers F-127 ($E_{100}P_{70}E_{100}$) (a) and P-123 ($E_{20}P_{70}E_{20}$) (b). Adapted with permission from P. Holmqvist et al.[37] (Copyright 1998, American Chemical Society).

The materials used in this thesis are based on the ternary system co-polymer, water and 1-butanol, extensively described by Lindman *et al*. as shown in Figure 3.1.[37-41] The polymer of choice is a non-ionic amphiphilic tri-block co-polymer formed by poly(ethylene oxide) (PEO) and poly(propylene oxide) (PPO) chains. Under the commercial name Pluronic®, several combinations of chain length and molecular architectures are available, F-127 ($PEO_{100}PPO_{70}PEO_{100}$) and P-123 ($PEO_{20}PPO_{70}PEO_{20}$) were the choice for this work. From the available range of self-assembled structures, we focused on two types which present anisotropy in their structures: the hexagonal and the lamellar phase (compositions detailed in the Table 3.1). The mixture was centrifuged to remove the air bubbles introduced during the mixing stage and stored at 4 °C overnight before further use.

Table 3.1. Compositions of the prepared self-assembled lyotropic liquid crystals in percentage by mass. The labels in the sample name refer to the self-assembled structure, being H_1 for Hexagonal and L_α for Lamellar.

Sample	Structure	F-127	P-123	H_2O	Butanol
FH_1	Hexagonal	35	-	50	15
FL_α	Lamellar	25	-	47.5	27.5
PH_1	Hexagonal	-	45	55	-
PL_α	Lamellar	-	75	25	-

3.2. Microfluidics Preparation

Microfluidics is a well-known tool for studying chemical reactions, physical processes and reproduce biological conditions. Typically, one or several channels with sizes in the micrometre range are produced in a bulk material through which a fluid flows under controlled conditions. The main advantage of microfluidic channels is the low sample volume, homogeneity in flow, and adaptability to a wide range of geometries. The confinement in the microscale produces a low Reynold's number where the viscous forces ensure a laminar flow with a smooth constant motion of the fluid. These conditions make it possible to study and predict some of the structure-related features in soft materials during flow such as phase transitions, ordering or segregation.

Microfluidic channels with low thickness, which offer a confinement in two dimensions, are frequently used together with microscopy and spectroscopy techniques to visualise the dynamics of fluids and suspensions in flow. Scattering techniques, specially using X-rays, allow to access to the nanostructural information and the radiation damage is minimized by the continuous flow in the channel which avoids long exposures to the high intensity radiation. However, the interaction of the scattering signal with the channel is often problematic, absorbing a considerable part of the scattered radiation or adding a big contribution to the background level. A suitable approach producing microfluidics compatible with synchrotron radiation was adapted from Lutz-Bueno et al.[42] in which a sandwich structure with glass and a layer of poly(imide) offers a high transmission and low background.

As shown in Figure 3.2, the process starts with the channel design transferred from a silicon hard mould to a flexible stamp. The silicon master was fabricated by photolithography on a 4 inches silicon wafer to obtain the negative patterns. The silicon master was used to produce several flexible stamps with positive features by soft lithography of poly(dimethyl siloxane) (PDMS). For this purpose, PDMS and crosslinker were mixed in the appropriate ratio and poured on the silicon hard mould followed by a degasification step with a rotatory pump to remove all the trapped air. the mixture was placed in an oven and baked at 70 °C for 60 min for the curing process.

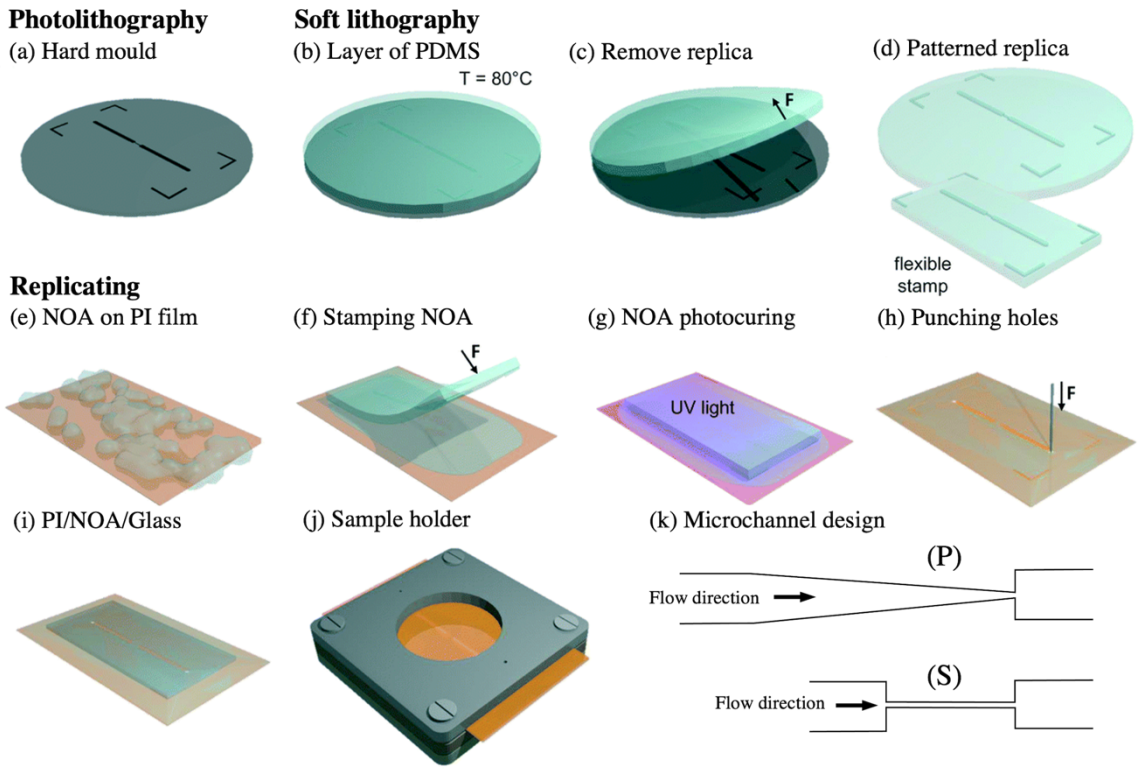

Figure 3.2. Fabrication process of the microfluidic channels compatible with synchrotron radiation (a-i). The lithographed silicon master (a) is used for the obtention of the flexible PMMA stamp (d). The channel design is stamped on the NOA layer (f) which is later photocured using UV light (g). The channels are mounted in an aluminium holder (j) which contains all the necessary connection. The selected designs (k) have a progressive (P) and sharp (S) contraction from 1.25 mm to a microchannel of 100 μm. Adapted with permission from Lutz-Bueno et al.[42] (Copyright 2016, Royal Society of Chemistry).

After obtaining the PDMS stamps, the following fabrication process was entirely performed in clean room conditions to prevent dust or other microparticles to block the channel. A polyimide (PI) film (25 μm thickness) (Goodfellow Corp., Cambridge, UK) was carefully cleaned with isopropanol and a droplet of UV curable resin (Norland Optical Adhesive, NOA#81) was poured on it. The PDMS stamp was pressed on the resin until the contact between the PI film and the stamp was reached and a pre-curing step was carried out. A UV lamp (365 nm) at a power of 6 mW/cm^2 for 12 seconds was used to partially cure the resin, after which the PDMS stamp was carefully removed, leaving the PI film with the resin spacer containing the pattern (i.e. the channel) stamped on it. After this, two holes were punched as

inlet and outlet, a glass cover slip was placed on top and the whole sandwich structure was exposed to UV radiation for 300 s to complete curing of the structure.

The selected designs for microchannels were intended to reproduce the two most commonly used 3D printing nozzles: blunt and conic, as shown in Figure 3.2i in the channels with the sharp (*S*) and progressive (*P*) contraction respectively. Both channels were designed with equal contraction ratio from 1.25 mm to 100 μm in width. The blunt channel has a straight channel as a sample reservoir of 1.25 mm width followed by a sudden contraction to 100 μm x 3.25 mm straight channel. The conic design has a similar wide channel as sample reservoir followed by a progressive contraction of 5 degrees to 100 μm with a total length of 6.5 mm. The thickness of the NOA layer defining the height of the channel was 250 μm for all the produced channels. The microfluidic channels and the necessary tubing were assembled in an aluminium holder which was fixed in the scanning SAXS setup. Syringe pumps (Cetony, neMESYS 290N) were used to have a controlled flow of 0.03, 0.30 and 3.00 μL/s during the whole experiment.

3.3. Small Angle X-ray Scattering (SAXS)

X-rays are electromagnetic radiation with a characteristic wavelength (λ) in the range of Ångströms (1 Å = 10^{-10} m). When an X-ray beam interacts with matter, different processes can occur. Most of the incident radiation will pass through the material without detectable interaction (transmission) and thus neither the X-rays direction nor their wavelength change. Another fraction will be absorbed and transformed in different type of energy (e.g. heat, fluorescence, etc). Lastly, a fraction will be scattered in other directions. When the scattered radiation has a different wavelength than the incident beam, it is considered inelastic or Compton scattering, which gives information of the atomic environment. If the scattered radiation has the same wavelength as the incident beam, elastic scattering occurs. The incident radiation interacts with the strongly bound electrons without energy transfer. This means that the electrons will oscillate with the same frequency as the incident radiation and therefore will emit photons at that frequency in all directions. The emitted waves of neighbouring atoms will give as a result an interference process in which radiation in the same phase will be amplified and in opposite phase will be muted. This results in an interference patter in the detector that carries structural information.

In a typical scattering experiment in transmission geometry (represented in Figure 3.3), the sample is exposed to an incident X-ray beam (defined by a vector $\overrightarrow{k_i}$) with wavelength λ. Some part of the radiation upon interacting with the sample will be scattered ($\overrightarrow{k_s}$) at an angle θ, which forms an angle 2θ with the incident beam. The intensity (I) of the scattered radiation is a function of the scattering angle (θ), which defines the scattering vector $\vec{q}$, defined as $\vec{q} = \overrightarrow{k_i} - \overrightarrow{k_s}$, which quantifies the length scale in the reciprocal space and relates with real space as shown in Equation 3.1. In case of elastic scattering $\vec{q}$ fulfils Bragg's law in Equation 3.2.

$$q = \frac{2\pi}{d} \qquad \text{Equation 3.1}$$

$$|\vec{q}| = q = \frac{4\pi}{\lambda}\sin\left(\frac{\theta}{2}\right) \qquad \text{Equation 3.2}$$

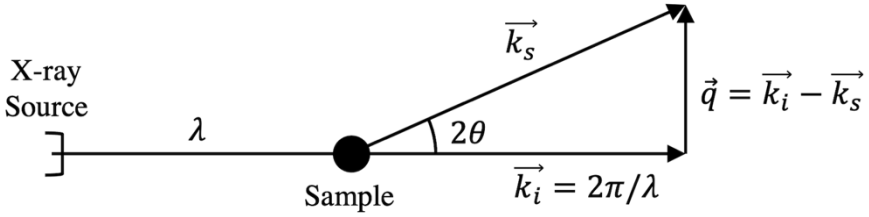

Figure 3.3. Schematic representation of a scattering experiment in a transmission set-up. The incident radiation is scattered by the atoms in the sample.

Small angle X-ray scattering (SAXS) is an analytical method to obtain structural information of materials with features in the nanometre range. In contrast with other scattering and absorption methods where the detector is placed a few centimetres from the sample, this technique is characterized by having a large distance (e.g. 2 - 50 m) between the detector and the sample. This detector placement allows for resolving the scattered radiation at lower angles which is the results of a smaller scattering vector and thus gaining information on relatively large structures. Using a 2D detector, not only the structure but the anisotropy of the material can be studied. As shown in Figure 3.4a, the scattering signal can be radially integrated in the whole azimuthal range, giving as a result the scattering intensity along the scattering vector. This information can be used to resolve the nanostructure of the material, periodicity and/or average size and shape of particles or fibres. On the other hand, the scattering intensity of a specific q-range can be evaluated across the azimuthal angle, as shown in Figure 3.4c. This type of analysis carries information about the anisotropy of the material. Materials with an isotropic and homogeneous structure will give as a result an isotropic scattering, while materials with some type of anisotropy will produce an anisotropic scattering pattern.

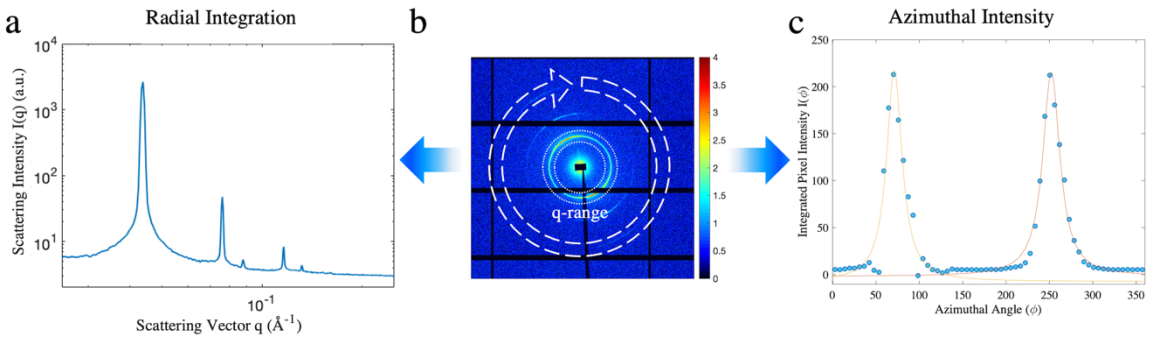

Figure 3.4. The analysis method in a SAXS experiment is based on the position of the scattering rings and their anisotropy (b). The signal can be radially integrated (a), to access the structural information or the azimuthal intensity evaluated (c) to analyse the anisotropy of the material.

The efficiency of the scattering process, the scattering length density (ρ) is dependent on the electron density of the atom (higher electron density means higher number of emitters).[43] The scattering intensity $I(q)$ depends on the contrast ($\Delta\rho$), which when using X-rays as a radiation source, is proportional to the difference between the electronic density of the sample and the environment. The intensity of the scattered radiation can also be expressed in terms of the so-called form factor $P(q)$ and structure factor $S(q)$. The form factor relates to the shape of the particle and polydispersity. The structure factor reveals the interaction between neighbouring particles e.g. electrostatic attraction/repulsion, when the distance between particles is in the same range as the size of the particles. In concentrated ordered systems where particles align themselves with certain periodicity (such in the liquid crystals studied in this thesis) the scattering signal can eventually develop a pronounced peak. This maximum in the scattering intensity is then called diffraction peak and its position reveal the distance between the scatterers according to Bragg's law (Equation 3.2).[43]

There are multiple data analysis strategies in order to study the nanostructure and anisotropy of the material. The phase of the self-assembled liquid crystal can be identified by the relationship between the diffraction peaks obtained.[37] Self-assembled crystalline phases with hexagonal periodicity follow the relationship $q'/q^* = 1{:}\sqrt{3}{:}2{:}\sqrt{7}{:}3{:}\ldots$ where q^* is the q-position of the first diffraction plane (01) and q' the q-position of the subsequent peaks. The lamellar phase follows in contrast the relationship $q'/q^* = 1{:}2{:}3{:}4{:}\ldots$

In scattering experiments, the main orientation direction can be directly calculated from the anisotropy of the scattering pattern. The degree of anisotropy can be evaluated by the alignment factor[44] or the degree of orientation.[45] Those parameters highly depend on the particle shape, since a perfectly aligned ellipsoid has a less pronounced anisotropy than a perfectly aligned thin rod. In the approach proposed by Bunk *et al.*[45] the scattering pattern is divided in N_θ azimuthal segments. The azimuthal intensity distribution can be approximated by a cosine function using the discrete Fourier transform of the intensities of each individual segment (n_θ), as shown in Equation 3.3. The baseline of the function (a_0) is the symmetric intensity, given by the average scattering intensity, and the amplitude of the signal (a_1) the asymmetric intensity, given by the anisotropy created in the scattering intensity as a result of orientation. The degree of orientation can then be defined as the relationship between the asymmetric and symmetric intensity in the scattering signal (a_1/a_0). The phase of the signal (θ_S) represents the actual angle of orientation in the reciprocal space. This method is not an order parameter, but a relative measurement of the degree of orientation. There are some limitations associated to the cosine approximation, which is not suitable for highly oriented materials such as the lyotropic liquid crystals studied in this thesis.

$$I \approx a_0 + a_1 \cos\left(\frac{2\pi n_\theta}{N_\theta} - \theta_S\right) \qquad \text{Equation 3.3}$$

The Hermans' orientation parameter instead uses the orientational order parameter discussed in Section 2.4, to quantify the anisotropy of the material.[46] The azimuthal intensity in the range -90° to 90° is normalized and interpolated by a Lorentzian curve (Figure 3.4c), centring

the peak position at 0°. According to the Hermans' algorithm, the Hermans' orientation parameter $\langle f_a \rangle$ is calculated using the Equation 3.4, where $I(\phi)$ is the intensity for each azimuthal angle (ϕ). The angle of the orientation is extracted by the peak position in the azimuthal intensity after the interpolation indicating the angle in the reciprocal space.[47]

$$\langle f_a \rangle = \frac{\int_0^{\pi} \left(\frac{3}{2}\cos^2\phi - \frac{1}{2}\right) \sin\phi \, I\phi \, d\phi}{\int_0^{\pi} \sin\phi \, I\phi \, d\phi} \qquad \text{Equation 3.4}$$

3.3.1. Scanning SAXS

By using a focused X-ray beam, high spatial resolution can be achieved. A highly intense beam interacts with a small volume of sample and additional motors that control the xy-plane (see experimental set-up in Figure 3.5a) raster scans the region of interest (ROI). As a result, one scattering pattern is obtained per scan point which is eventually analysed to form the image containing the structural information about the sample. Due to the small volume of probed sample, high intensity sources are required to measure in reasonable times and provide small enough beam sizes. Therefore, scanning SAXS experiments are mostly performed at synchrotron facilities, which offer high flux and a focused beam. The short exposure times make this method a perfect combination to study large areas with small step size and visualize dynamic processes such as time-resolved *in situ* experiments.

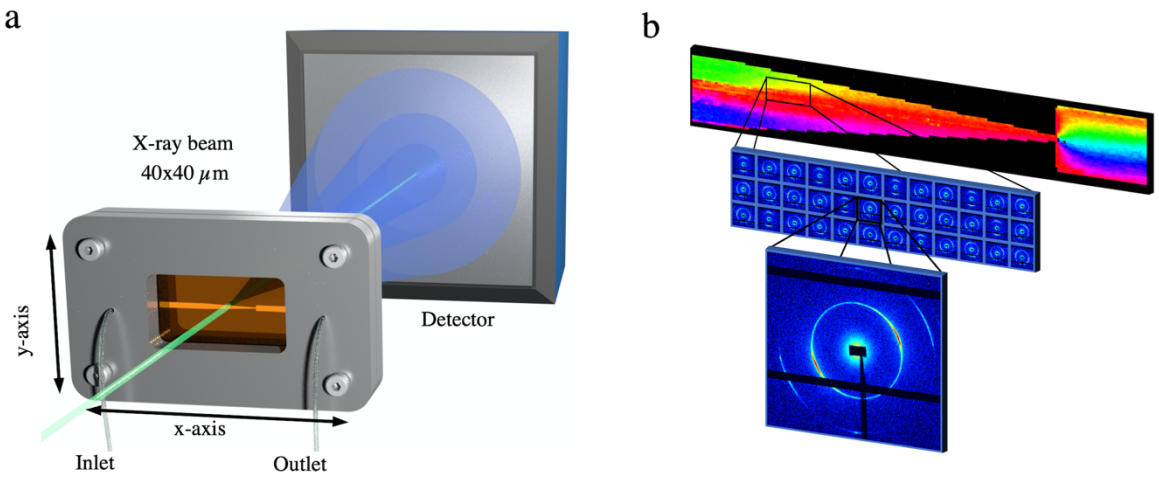

Figure 3.5. a) Schematic representation of a scanning scattering experiment with microfluidics in a transmission set-up. The microfluidic channel is raster scanned through a focused X-ray beam in the xy-plane and the scattering is registered by a 2D detector in each pixel. b) The scattering signal in each scan point is later processed and the information colour coded in a 2D map for an easy interpretation.

The scanning SAXS experiments presented in Paper I and II were performed at the coherent small-angle X-ray scattering (cSAXS) beamline at the Paul Scherrer Institute (PSI, Switzerland). A focused X-ray beam (40x40 μm) was monochromated by a fixed-exit double crystal Si(111) monochromator to an energy of 11.2 keV (1.107 Å). A flight tube with a length

of 2 m was placed between the sample and the detector to minimize the air scattering and absorption. The transmitted beam was measured with a photodiode on a beamstop, placed inside the flight tube and the scattering signal was recorded by a Pilatus 2M detector after the flight tube.[48] The exposure time in the microfluidic experiments was 0.20 s and the in-situ 3D printing 0.08 s at a sample-to-detector distance of 2.158 m, which was calibrated with silver behenate. The data analysis was performed by calculating the Hermans' orientation parameter and angle of orientation in each scanning point. The principal diffraction peak in both samples, which corresponds to the cylinder/lamella interspace (see Figure 2.1) was also fitted from which the peak position, width and amplitude were obtained.[45]

3.4. Rheology

Rheology is the branch of science that studies the deformation and flow of matter and aims to relate the macroscopic behaviour with the nanoscopic structure. Two common ideal states for matter are perfectly elastic solids and ideal viscous liquids. Real materials are far from ideal, and especially soft matter commonly presents a complex behaviour, which is called viscoelasticity. Elasticity is the ability of resisting a deformation caused by a force, returning to the original shape when it is released. In general terms, it is generated by strong but flexible bonds in the atomic structure. Viscosity in contrast is the flow resistance caused by internal friction of molecules or particles with non-permanent bonds when they are forced to move from their equilibrium positions. The viscosity (η) is usually defined in systems with shear where it is dependent on the shear stress (σ) and the velocity gradient or shear rate ($\dot{\gamma}$) as in Equation 3.5. The shear viscosity can have two different behaviours. If the viscosity is independent of the shear rate, it is considered a Newtonian fluid. However, when the viscosity depends on the shear rate, the fluid is considered non-Newtonian and its response becomes not linear.[49]

$$\sigma = \eta\dot{\gamma} \qquad \text{Equation 3.5}$$

A common way to measure the viscoelastic behaviour is through oscillatory tests, in which the sample is sheared between two plates with small amplitude oscillations at different frequencies. In such measurements the upper plate oscillates with a given stress or strain amplitude and at a given frequency. The movement can be represented by a sinusoidal wave in time with the stress or strain as the amplitude. If the stress is controlled, the plate applies a torque and the displacement is measured. In a strain-controlled experiment, the angular displacement is controlled and the necessary torque to reach that displacement is measured (from where shear stress is calculated). The result of these experiments is the complex modulus (G^*) which measure the resistance of deformation (stiffness) as in Equation 3.6. The elastic component of the complex modulus (storage modulus: G') represents the stored elastic energy and the viscous component (loss modulus G'') the energy lost during the deformation due to internal friction of the fluid. In the mathematical description of the complex modulus, the storage and loss moduli are the representation of the real and imaginary parts,

respectively. From this expression the complex viscosity (η^*) can also be defined in Equation 3.7 such as the total resistance to flow as a function for the angular frequency of the oscillation (ω).[50]

$$G^* = G' + iG'' = \frac{\sigma_{max}}{\gamma_{max}} \qquad \text{Equation 3.5}$$

$$\eta^* = \eta' + i\eta'' = \frac{G^*}{\omega} \qquad \text{Equation 3.7}$$

The rheological characterization of the lyotropic liquid crystals used in Paper I and Paper II was carried out using an Anton Paar MCR702 TwinDrive rotational rheometer in a separate motor-transducer (strain-controlled) configuration. The viscoelastic modulus in paper I and viscosity curves in Paper I and Paper II were obtained by oscillatory and steady shear measurements. A configuration of parallel plate geometries of 25 mm in diameter were used for all the experiments with the exception of the oscillatory tests in the hexagonal liquid crystal of the polymer F-127, where parallel plates of 7 mm and 15 mm were used. Strain sweep tests were performed at 1.0 rad/s for a shear strain amplitude range from 0.02 to 200 %. Frequency sweep test were performed at angular frequencies, with a constant strain amplitude of 0.01 % in the linear viscoelastic range, as determined from the strain-sweep tests. The steady shear tests were performed at a shear rate from $9.0 \cdot 10^{-4}$ to 30 s^{-1}.

3.5. Birefringence Microscopy

The optical property of a material, which has a refractive index that depends on the polarization and propagation direction of the light, is called birefringence. Birefringent materials are characterised by having double refraction, which produces a double transmitted beam of light with opposite polarization in two different paths (see Figure 4.6). One of the two split beams travels through a shorter path and therefore faster, which is called the ordinary ray. The other one is dependent on the propagation direction, taking a longer path and traveling slower, and is called extraordinary ray. Birefringence (B), in Equation 3.8, is then the difference of the extraordinary (n_e) and the ordinary (n_o) refractive index. The ordinary ray will reach the highest velocity when the polarization is parallel to the optical fast axis, which indicates the direction of the optical anisotropy.

$$B = |n_e - n_o| \qquad \text{Equation 3.8}$$

The relationship between the phase and the velocity of both transmitted rays is calculated trough the retardation (Γ). The retardation is a measure of how much the slow ray will be retarded with respect the fast ray due to the orthogonal polarization between both rays. It can be calculated taking into account the birefringence and the thickness (t) of the sample as:

$$\Gamma = \mathrm{t} \cdot |n_e - n_o| \qquad \text{Equation 3.9}$$

Birefringence in polymeric materials is the consequence of the optical anisotropy caused by the orientation of polymer chain segments by natural or artificial processes such as flow.[51] At a higher hierarchical level, supramolecular organization can produce form birefringence when particles with anisotropic shapes are in a media with a different refractive index. Isotropic structures such as polymeric micelles are not birefringent, however more complex structures such as agglomerations of micelles, cylinders, worm-like micelles or crystal-like structures with anisotropy in at least one dimension can develop optical anisotropy.[52, 53] Birefringence microscopy is a useful technique to study ordered polymeric materials with spatial resolution. This method allows to obtain the retardance and angle of the fast axis in each pixel, which makes possible to quantify the degree and orientation of the anisotropy.

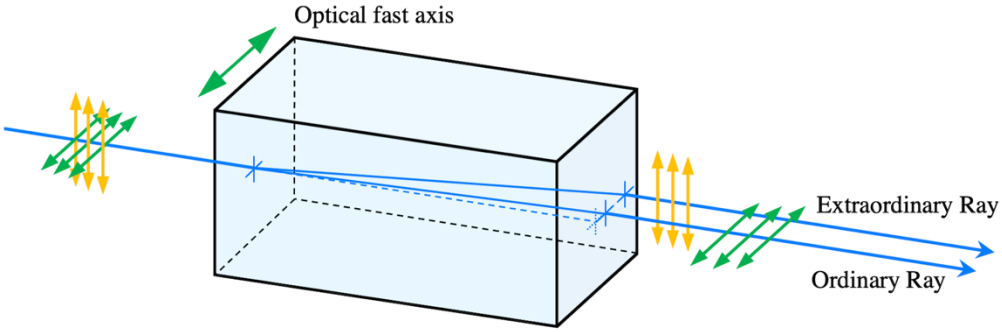

Figure 3.6. Scheme of the birefringence principle in an optically anisotropic material. The incident ray is split in two rays with different optical paths and polarization angles depending on the optical fast axis of the material.

Birefringence microscopy was used to quantify the retardance and angle of the optical fast axis of the presented lyotropic liquid crystals using the imaging system Exicor Birefringence MicroImager™ (Hinds Instruments, Inc., OR). The optical set-up consists of a linear polarizer at 0°, a photoelastic modulator (PEM) at 45°, a PEM at 0° and a linear polarizer at 45°. The samples are placed in the image stage between the two PEM and measured with an objective of 10x and 20x in a 2048 x 2048 pixel 12-bit CCD camera which created a field of view of 1 mm x 1 mm and a spatial resolution of 0.50 μm/pixel and 500 μm x 500 μm with 0.25 μm/pixel respectively. A stroboscopic LED source with a wavelength of 475 nm was used to calculate the Mueller matrix components ($P_{m,n}$) and provide quantitative measurements of the sample retardance Γ (Equation 3.10) and angle of the optical fast axis θ (Equation 3.11) in the field of view.[54, 55] The angle of the fast axis is color-coded from -90° to 90° for easier interpretation.

$$\Gamma = \arctan\sqrt{(P_{13}/P_{33})^2 + (P_{23}/P_{33})^2} \qquad \text{Equation 3.10}$$

$$\theta = 0.5\arctan(P_{13}/P_{23}) \qquad \text{Equation 3.11}$$

Chapter 4

Results and Discussion

This chapter contains the results included in Papers I and II. A general overview of the self-assembled materials used in the experiments is followed by two separated parts: confined and open flow. Nanostructure and anisotropy are at the focus of this chapter, which are visualised employing imaging techniques such as scanning SAXS and birefringence microscopy. The experiments are complemented with rheology measurements, which helped understanding the processes that led to the different degrees of anisotropy and observed nanostructures.

4.1. Self-assembled structure of lyotropic liquid crystals

The results shown in this thesis are centred around the self-assembled system containing an amphiphilic molecule, water and butanol, forming a lyotropic liquid crystal. This ternary system is based on the tri-block co-polymer poly(ethylene oxide)-poly(propylene oxide)-poly(ethylene oxide) (PEO-PPO-PEO) in which the chain length of each block was either $PEO_{100}PPO_{70}PEO_{100}$ (Pluronic® F-127), which was labelled as polymer *F*, or $PEO_{20}PPO_{70}PEO_{20}$ (Pluronic® P-123), which was denoted as polymer *P*. These polymers offers a wide variety of possible phases as first described by Holmqvist et al.[37], the hexagonal and lamellar structures were selected for this study due to their anisotropy and periodicity in two and one spatial dimensions, respectively.

4.1.1. Small Angle X-ray Scattering

Small angle X-ray scattering was used to study the nanostructure of the lyotropic liquid crystals and evaluate their mesoscopic order. A representative radial integration of the scattering signal from the SAXS measurements carried out in the microfluidics channels in Paper I and the *in situ* 3D printing in Paper II are shown in Figure 4.1. The diffraction peaks prove long range order, the phase can be deduced by calculating the ratio between the diffraction peak positions. Following the ratio polymer:water:butanol detailed in Section 3.1, Table 3.1, the liquid crystals produced using polymer *F* with composition 35:50:15 and *P* with 45:55:0 have a peak ratio of 1:√3:2:√5:4 (Figure 4.1 blue line) which reveals a hexagonal system (H_1). These two materials are therefore labelled as FH_1 and PH_1 respectively. Due to the amphiphilic character of the polymer, it assembles in a cylindric arrangement with the hydrophobic PPO block in the inner part and the hydrophilic PEO block towards the water media (Figure 4.2a). The cylinders are further assembled in a 2-dimensional hexagonal lattice

(Figure 4.2b) with cylinder interdistance of 165.4 Å and 151.4 Å for FH_1 and PH_1, respectively as determined from the first diffraction peak.

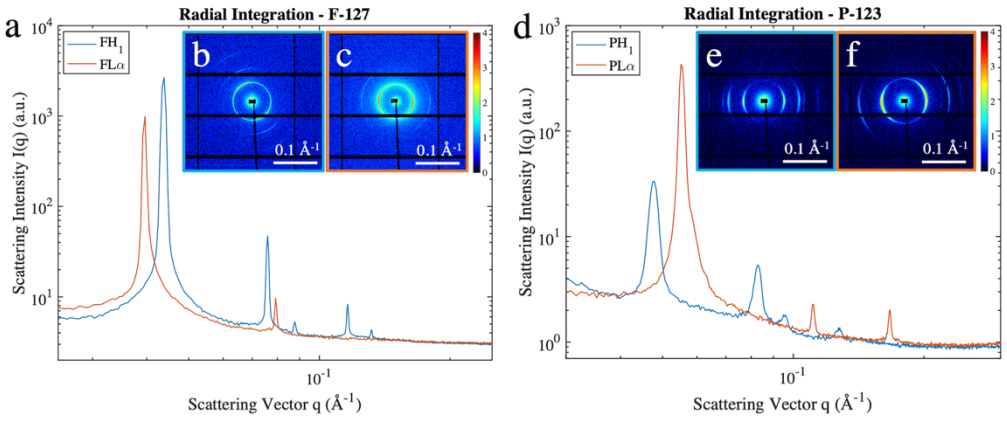

Figure 4.1. Radial integration obtained in the SAXS experiments of the lyotropic liquid crystals in hexagonal (H_1) and lamellar (L_α) phase for the polymer F-127 (a) and P-127 (d). The insets show the 2D scattering patterns recorded for the hexagonal (b, e) and lamellar (c, f) self-assembled structures.

The lyotropic liquid crystals prepared with the composition 25:47.5:27.5 for polymer *F* and 75:25:0 for polymer *P* have a peak ratio of 1:2:3 (Figure 4.1 red line), characteristic for a lamellar self-assembled structure (L_α). The polymers create bilayers in a lamellar stack with the PEO blocks facing the water media and the PPO block the inner part of the bilayer (Figure 4.2d), which have an order in the nanometre range, but are considered to have infinite lateral dimensions.[39, 56] Those samples were therefore denoted as FL_α and PL_α, which have an interlamellar dimension of 159.5 Å and 113.9 Å, respectively (Figure 4.2e).

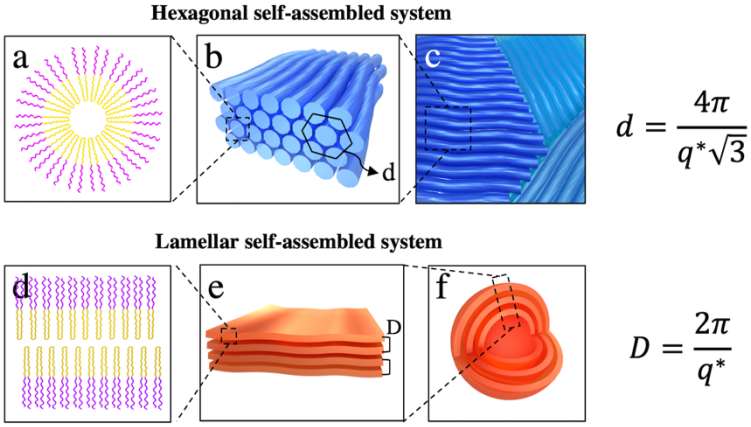

Figure 4.2. Triblock co-polymer in cylindrical cross-section (a), self-assembled in in cylindric micelles in a hexagonal lattice (b) with cylinder distance *d*. The cylinders can eventually form microdomains with different relative orientations (c). The amphiphilic polymer can for bilayers (d) as well, may create extended lamellae (e) or multilamellar vesicles (f), with interlamellar distance *D*. The pink and yellow parts in (a) and (d) corresponds to the hydrophilic and hydrophobic blocks respectively in the tri-block co-polymer. q^* represents the value of the scattering vector in the first diffraction peak, which corresponds to the crystalline plane (100).

4.1.2. Rheological characterization

Oscillatory tests of the self-assembled liquid crystals were performed to reveal the rheological behaviour of the hexagonal and lamellar phases. The linear viscoelastic storage (*G'*) and loss (*G''*) moduli (Figure 4.3a-b) were measured in a frequency sweep for a constant strain rate (γ) of 0.01 % within the linear viscoelastic regime. For both hexagonal and lamellar phases, the response is dominated by the elastic component, $G' > G''$. The moduli are independent of the angular frequency and parallel between each other, which is characteristic of a gel-like behaviour with the exception of FL_α, which has a trend to a more fluid-like characteristic with convergent slopes.[57] The rheological response of these materials is dominated by the interaction between the self-assembled structures.[58]

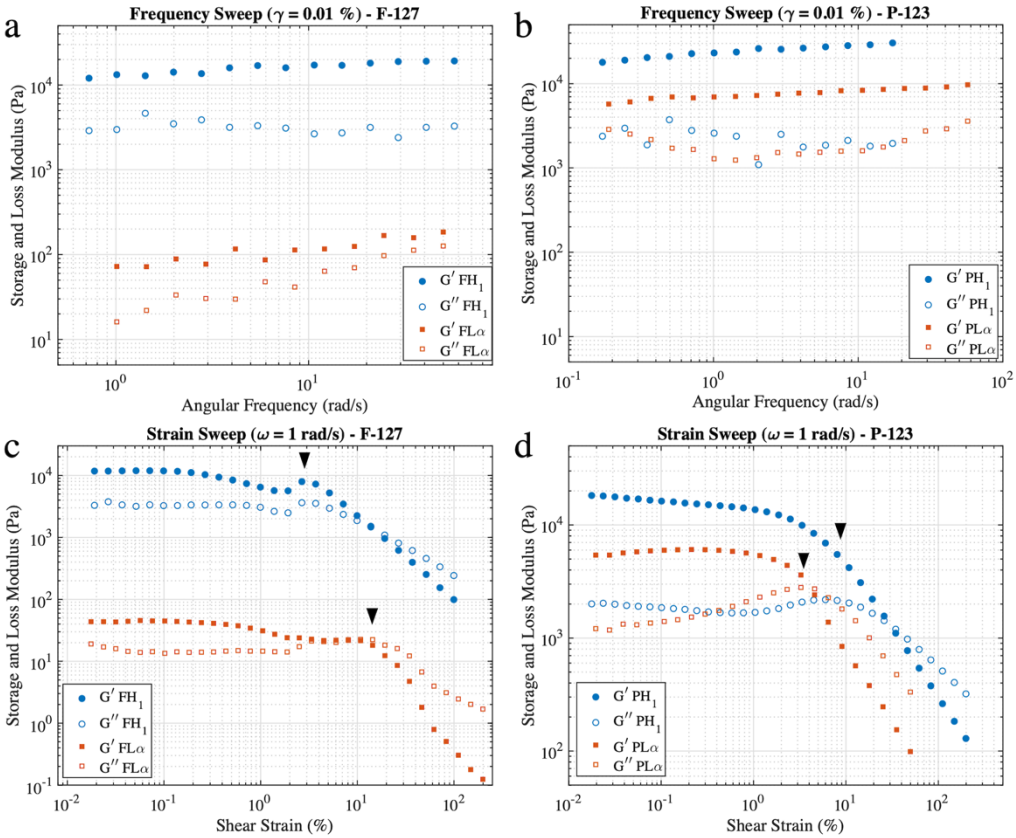

Figure 4.3. Rheology characterization of the liquid crystals measured by oscillatory tests. The storage (*G'*) and loss (*G''*) moduli are represented for the frequency and strain sweeps of the hexagonal and lamellar phases of polymers F-127 (a-b) and P-123 (c-d). For an easier comparison, the viscoelastic moduli in the frequency sweep is shown with the same scale. Black arrows indicate the point where strain overshoot can be identified.

Figure 4.3c-d represents the strain sweep of the liquid crystals for an angular frequency (ω) of 1.0 rad/s. Beyond the linear viscoelastic regime, there are two characteristic behaviours characterised by an increase in the loss modulus and/or the storage modulus. An increase in both *G'* and *G''*, as seen for FH_1, is known as strong strain overshoot.[59] It is related with intermolecular interactions between the polar chains in large ordered materials, which could be explained as cluster size growth of hexagonally packed cylinders with a common

orientation.[59-61] The movement and reorientation of cylinder aggregates produce an increase in the size of the clusters with a preferential orientation towards the direction of the movement. As a consequence, *G'* and *G''* increase, which for high strain amplitudes when *G'' > G'*, aggregates tend to break and reorient in the direction of movement. For PH_1, only the loss modulus increases, which is known as weak strain overshoot. This type of behaviour is characterised by an increase in the loss modulus *G''*, which is produced by a resistance to deformation of the self-assembled structure by the movement of the fluid. After a critical point, the stress is able to deform and realign the structure in the direction of the movement, however in this case cluster break-up is not considered, due to stronger interaction between their building blocks.[62] In the case of the lamellar phases of both polymers, FL_α and PL_α, weak strain overshoot is also observed, with an increase in the loss modulus, related with energy dissipation. For lamellar systems, weak strain overshoot is related to layer-to-layer sliding, caused by shear stress in the fluid.[60, 63] At high shear rates G'' becomes higher than G' during the nanostructure reorganization. From that point on, the viscoelastic moduli decrease, and the material flows more easily.

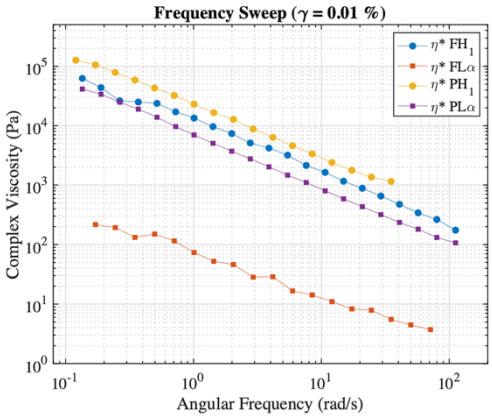

Figure 4.4. Complex viscosity (η^*) of the hexagonal and lamellar phases obtained by oscillatory tests in a frequency sweep for a strain rate of 0.01 %.

The complex viscosity of the hexagonal and lamellar self-assembled crystals was obtained by a frequency sweep with a constant strain of 0.01 % measured in the linear viscoelastic regime. Figure 4.4 shows a shear thinning behaviour, with a viscosity that decreases with the applied frequency. Both phases present a similar slope with a general higher viscosity in the hexagonal phase and a notable low viscosity for FL_α. The low viscosity of that crystal makes it interesting to study its behaviour under flow. Compared to the equivalent hexagonal self-assembled phase however, FL_α. is not suitable for 3D printed since it cannot keep the extruded shape. For that reason, the following results are divided in two parts. Confined flow inside the nozzle was studied with the hexagonal and lamellar phases of the polymer *F*. Open flow and *in situ* 3D printing was studied using the materials with a high enough viscoelastic modulus that allowed them to keep the extruded shape, e.g. FH_1, PH_1 and PL_α.

4.2. Confined flow and anisotropy

4.2.1. Influence of the flow rate and channel design

The rheology experiments shown in the previous section indicate the effect of shear in the prepared lyotropic liquid crystals, using microfluidic channels to reproduce the 3D printing nozzles allows to study more complex flows with shear and extensional contributions. Scanning small angle X-ray scattering (SAXS) was used to study the structure and anisotropy of the self-assembled systems in the confined space of the microfluidic channels (see set-up schematics in Figure 3.4a). As described in more detail in Chapter 3.2 two microchannel designs were used to mimic the most common 3D printing nozzles, conic and blunt. The channels were prepared with the same contraction ratio from 1.25 mm to 100 μm, using a progressive and a sharp contraction as shown in Figure 4.5a. The hexagonal and lamellar phases of the polymer *F* were pumped through at a constant flow rate of 0.03, 0.30 and 3.00 μL/s. During the flow, the channels were scanned by the X-ray beam and the Hermans' orientation parameter, peak width and peak position of the main diffraction peak (Figure 4.1a) were averaged in the first 400 μm before the end of the contraction, indicated by the coloured dashed square in Figure 4.5a.

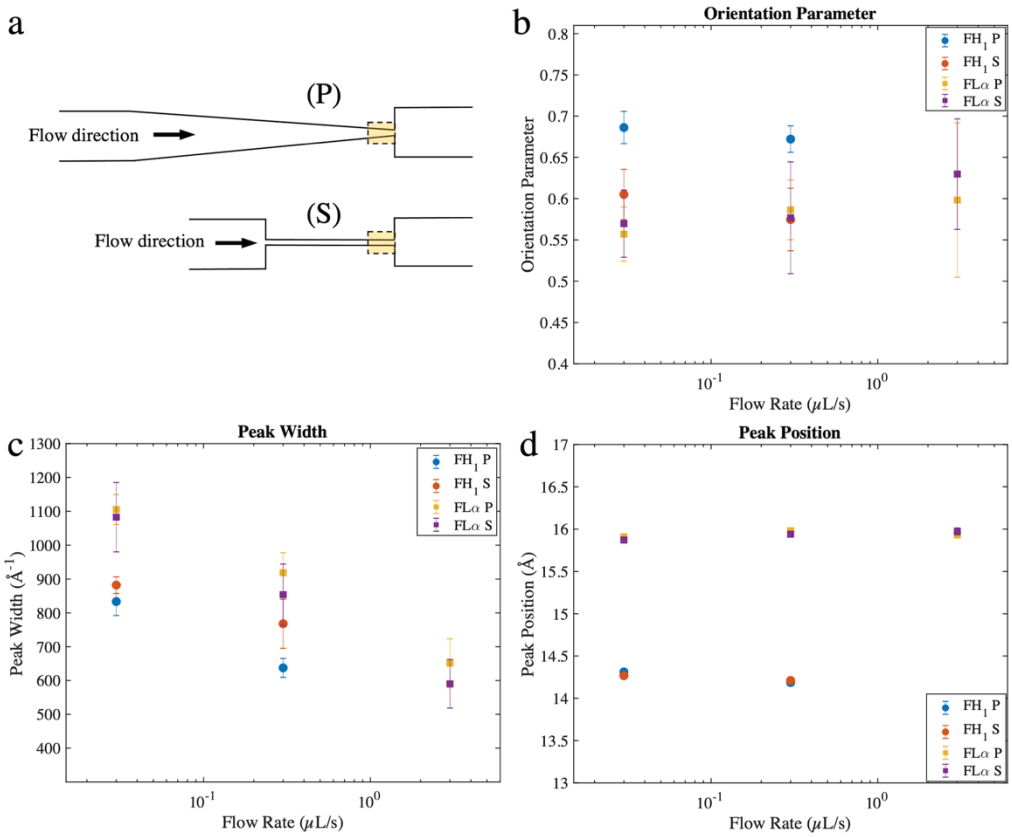

Figure 4.5. a) Scheme of the microfluidic channels used with a progressive (P) and sharp (S) contraction. The yellow dashed box (length: 400 μm) shows the area where the Hermans' orientation parameter (b), peak width (c) and peak position (d) were averaged.

The average Hermans' orientation parameter of the hexagonal phase FH_1 in the progressive contraction is $\langle f_a \rangle^P_{FH_1} = 0.68 \pm 0.01$ compared to $\langle f_a \rangle^S_{FH_1} = 0.59 \pm 0.02$ in the sharp one. The lamellar phase FL_α presents no significant difference with an orientation parameter of $\langle f_a \rangle^P_{FL\alpha} = 0.58 \pm 0.04$ and $\langle f_a \rangle^S_{FL\alpha} = 0.59 \pm 0.03$. The orientation parameter of the hexagonal phase does not increase with the flow rate, which fluctuates around the commented value, however it slightly increases for the lamellar phase up to 0.60 in the progressive and 0.63 in the sharp contractions (Figure 4.5b). The peak width decreases with the flow rate (Figure 4.5c), which is probably caused by an enlargement of the crystalline domains due to the reduction of the available space and increase of the fluid velocity, which improved the long-range order. The peak position in Figure 4.5d stays constant at a d-spacing of 14.2 Å for FH_1 and 15.9 Å for FL_α. This lack of fluctuation demonstrates the stability of the self-assembled phases at the lower hierarchical scale within the confinement. Peak shits related with changes in the cylinder or lamella interspace were not observed due to changes in the studied flow rates.

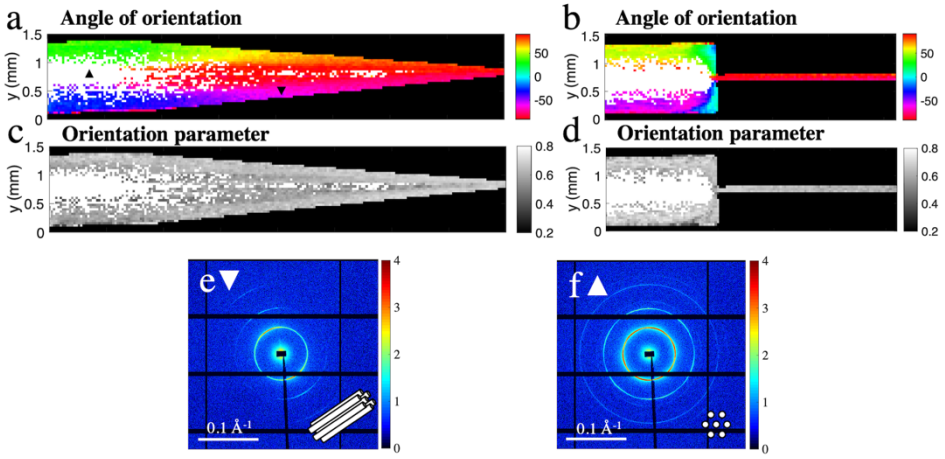

Figure 4.6. Scanning SAXS measurements of the lyotropic liquid crystal in the hexagonal phase (FH_1) in the microfluidics channel with a flow rate of 0.03 μL/s. Flow direction from left to right. Scattering pattern from a pixel where the orientation of the domain is e) perpendicular (▼) and f) parallel (▲) to the beam. The angle of orientation of the scattering is colour coded according to the colour scale from -90° to 90°.

Figure 4.6a-d show the angle of orientation and the Hermans' orientation parameter of the hexagonal FH_1 liquid crystal in the microfluidic channel at a flow rate of 0.03 μL/s. The scattering intensity of the diffraction peaks was evaluated in the azimuthal angle for each scanning point (i.e. pixel). Some channel regions had two intensity maxima corresponding to the scattering signal of cylindric micelles parallel to the channel plane (Figure 4.6e). The central area of the channel showed a scattering pattern with 6 maxima in the azimuthal angle (Figure 4.6f). This type of diffraction signal in a hexagonal 2D lattice is expected when the crystalline long axis is oriented parallel to the beam.[20,64] Thus, the crystalline domains in these regions are oriented perpendicular to the flow direction. The scattering pattern found in these scan points is not compatible with the orientation quantification by the Hermans' algorithm therefore the corresponding pixels were masked out in white. The angle of orientation and orientation parameter are comparable in both channels. They reach an angle in the range of ±

3 degrees with a higher oriented layer in the proximities of the walls. The velocity profile in that area is expected to be lower, however the shear rate is maximized. The use of a contraction increases the extensional flow in the centre of the channel, which plays an important role in the alignment of particles in flow. However, the perpendicular orientation found in the central area contradicts the expected orientation. We presume that shear is playing a major role in the alignment and the shear rate is not high enough to orient the liquid crystal in that region.

The orientation in the lamellar phase FL_α occurs already more downstream with a more uniform distribution in the channel area and high alignment values at the entrance of the channel as shown in Figure 4.7a-b. This can be connected to the lower viscosity of the lamellar phase and a lower resistance to movement and orientation in the flow direction as discussed in Section 4.1.2. The orientation parameter in Figure 4.7c-d shows three areas with different values. Area A has a high orientation parameter in the proximities of the walls, which decays to a minimum in area B and then slightly increases in the centre of the channel in area C, as illustrated in Figure 4.7c and Figure 4.7e. The shear rates in the walls are maximum as explained in the previous case with the hexagonal phase.

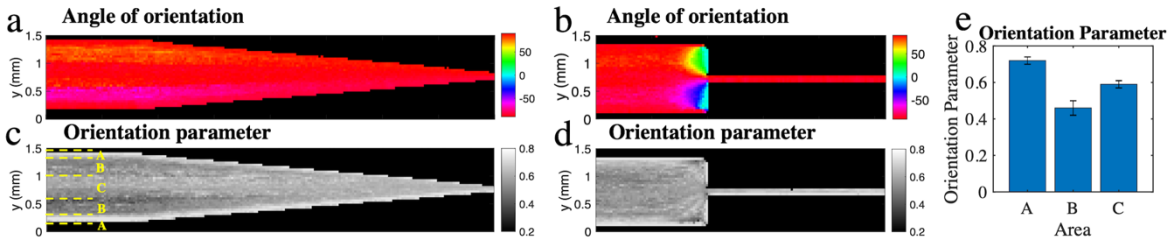

Figure 4.7. Scanning SAXS measurements of the lyotropic liquid crystal in the lamellar phase (FL_α) in the microfluidics channel with a flow rate of 0.03 μL/s. Flow direction from left to right. The angle of orientation of the scattering is colour coded according to the colour scale from -90° to 90°. The areas indicated with the letters A, B and C correspond with the three regions found in the orientation parameter.

4.2.2. Morphological changes during flow

In order to investigate the different regions of alignment a more in-depth study of the rheological behaviour of the liquid crystals was done by steady shear measurements. The viscosity dependence of the shear rate is shown in Figure 4.8. FH_1 has a uniform viscosity curve with a shear thinning character. In contrast, FL_α has a viscosity curve with three different slopes in the experimental data. In order to relate the measured viscosity and the microfluidic experiments previously shown, the approximate shear rate in the microchannels was calculated using Son's model.[65] It uses the width (W), height (H) and flow rate (Q), and it is applicable to micellar systems[66] in geometries when the velocity is dependent of the lateral dimensions ($W \approx H$). This model calculates the apparent shear rate ($\dot{\gamma}_a$) in Equation 4.1 and the wall shear rate ($\dot{\gamma}_w$) in Equation 4.2, where f^* is a tabulated function

dependant of the ratio height/width and n is the power law index (see Paper I). The calculated wall shear rate ($\dot{\gamma}_W$) is found in the regime III of the viscosity curve.

$$\dot{\gamma}_a = \left(\frac{6Q}{WH^2}\right)\left(1+\frac{H}{W}\right)f^*\left(\frac{H}{W}\right) \qquad \text{Equation 4.1}$$

$$\dot{\gamma}_w = \dot{\gamma}_a\left(\frac{2}{3}\right)\left(\frac{b^*}{f^*}+\frac{a^*}{f^*}\frac{1}{n}\right) \qquad \text{Equation 4.2}$$

Figure 4.9 shows the scattering pattern of representative pixels in the three areas of the microchannel. Close to the channel walls, at high shear rates (area A and regime III of the viscosity curve), the diffraction peak associated to the lamella interspace shows a strong anisotropy, which indicates aligned extended lamellae perpendicular to the shear plane in accordance with previous literature.[56] In the intermediate area (area B and regime II), the diffraction peak appears at the same q-value but with an isotropic intensity in contrast to area A. This is an intrinsic feature of vesicular systems, which consist of spherical bilayers with homogeneous wall thickness and low anisotropy. The area C has a scattering pattern with a diffraction peak in the whole azimuthal range, however the intensity is not homogeneous. This scattering pattern is expected from elongated vesicles. The shear rate in the centre of the channel is significantly lower, but the contraction induces a high extensional flow. Thus, vesicles are stretched towards the contraction.

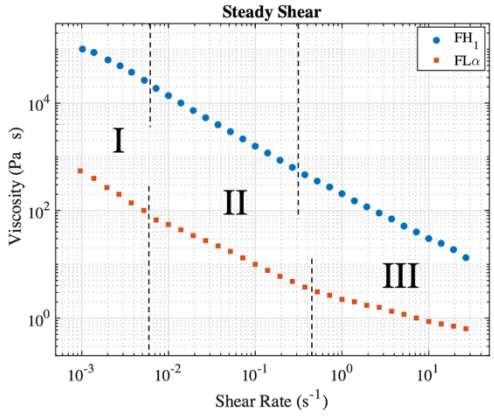

Figure 4.8. Steady shear measurements of the hexagonal and lamellar self-assembled phases. The viscosity dependence of the shear rate is split by the dashed lines in the three different slopes found.

These findings are supported by other studies on co-polymers self-assembled in lamellar structures which have also shown a viscosity curve with three regimes.[67] At low shear rates (regime I) the structure has a high number of defects such as dislocations in the lamellas. The viscosity regime I is likely dominated by local re-arrangements in the microstructure without significant conformational alterations. At intermediate shear rates (regime II), the formation of multilamellar vesicles has been discussed, which are broken into extended lamellae at high shear rates.[67] Multilamellar vesicles are likely to be formed due to the movement and wrapping of extended lamellae during the local reorientation, which are stretched due to the flow until they break and form well-ordered lamellae at high shear rates (regime III).

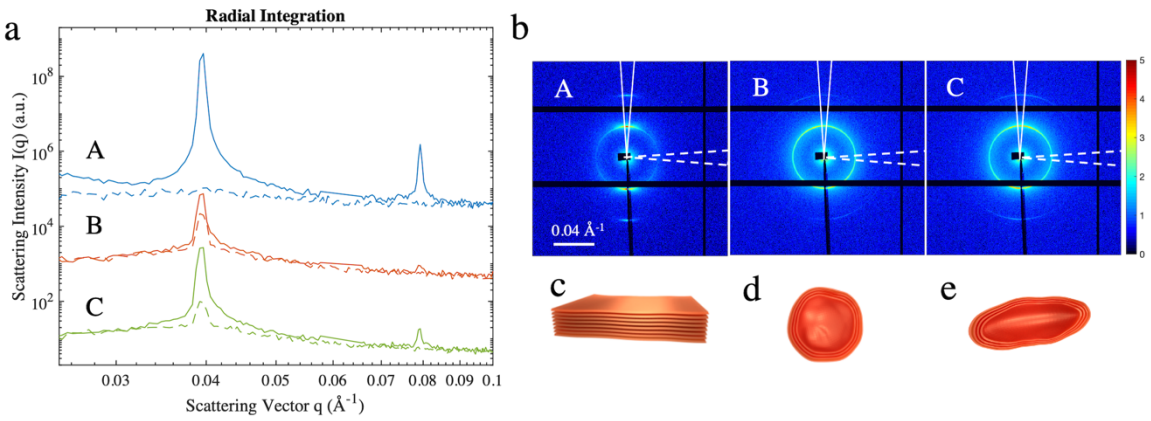

Figure 4.9. a) Radial integration in two segments with a difference of 90° plotted in solid and dashed line. b) Scattering pattern of a representative point in the three identified areas in Figure 4.7c. The scattering seen in A correspond to extended lamellae (c), whereas B shows the scattering of multilamellar vesicles (d) and C multilamellar vesicles stretched in the flow direction (e). The curves have been shifted vertically for better clarity.

4.3. *In situ* 3D printing and study of the induced anisotropy

After the analysis of the anisotropy and nanostructure of the materials in confined flow, a further step into open flow conditions is necessary to get a more complete overview of the induction of alignment in 3D printing as well as their evolution after exiting the nozzle. As discussed before in Section 4.1.2, only the lyotropic liquid crystals with a high enough viscoelastic modulus are appropriate for 3D printing. The samples FH_1, PH_1 and PL_α were loaded in the 3D printer cartridge and extruded while being scanned *in situ* by the X-ray beam. The results in Figure 4.10 show that the hexagonal structures have a higher orientation parameter when extruded through a larger nozzle diameter (Figure 4.10a-e). The average orientation parameter increased a 30 % for FH_1 and 38 % for PH_1 from the smallest to the largest nozzle, with a maximum mean value of $\langle f_a \rangle^{FH_1} = 0.64 \pm 0.06$ and $\langle f_a \rangle^{PH_1} = 0.61 \pm 0.02$ respectively. The lamellar structure PL_α is in contrast not significantly influenced by the nozzle diameter, with maximum mean value of $\langle f_a \rangle^{PL_\alpha} = 0.50 \pm 0.11$ (Figure 4.10f-h).

The filaments show a core-shell structure with a higher orientation parameter in the outer layer and a low oriented core. As explained in Section 4.2.1, the shear rate in the proximities of the walls is higher than in the middle, which influences the orientation parameter. High viscosity fluids with shear thinning behaviour (see Figure 4.4) can create a plug flow with a highly oriented layer that creates a shield effect in the rest of the filament where the internal core is then pushed by the surrounding material. In cylindrical deposition nozzles, a thin skin layer is followed by a yielded shell that experienced high shear forces. In the core of that filament, an unyielded gel moves at a constant velocity pushed by the flow.[68] This thin skin layer with high orientation is in particular distinct for PH_1 at 460 µm (Figure 4.10d)

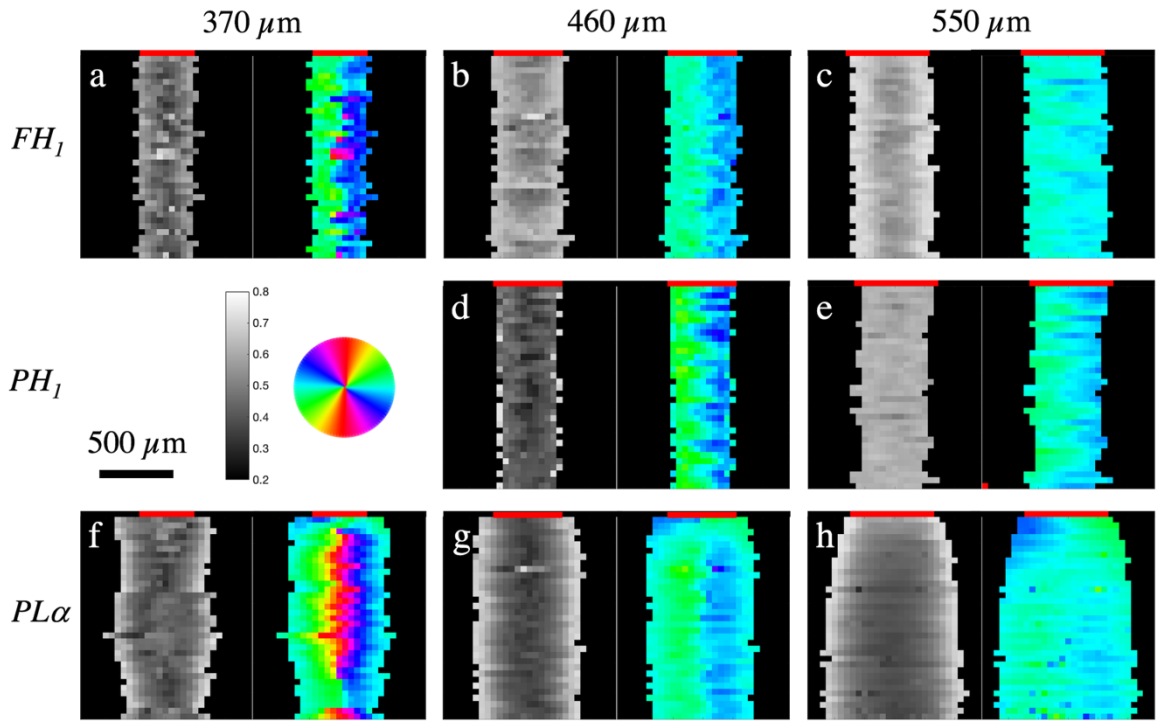

Figure 4.10. Scanning SAXS of the *in situ* 3D printed lyotropic liquid crystals increasing nozzle diameters (left to right). The Hermans' orientation parameter (left) and angle of orientation (right) was calculated and color-coded for an easy interpretation. The internal diameter of each nozzle is represented by a row of red pixels on the top of the scanning maps.

The average angle of orientation of the scattering signal is in the range of ± 5°, which corresponds to the alignment of the hexagonal rods (Figure 4.2a-e) and lamellar sheets (Figure 4.2f-h), respectively, in the direction of extrusion. The variation of the angle of orientation is also strongly correlated with the nozzle diameter. Filaments produced by larger nozzle diameters have a more homogeneous alignment (turquoise) as well as a higher orientation parameter. Smaller nozzles created a distinct pattern of alignment directed diagonally downwards from each side of the wall (blue and green, respectively) in a V-shape for the 460 μm nozzle (Figure 4.10b, d and g) and U-shape for the 370 μm nozzle (Figure 4.10f).

4.4. Phase transformations, relaxation and evolution of the alignment

The use of inks which are based on solvents, are susceptible of evaporation during the manufacturing process. The evaporation may change their properties due to the change in the composition, which defines the self-assembled structure of the lyotropic liquid crystals. Birefringence microscopy of the 3D printed filament was carried out to observe possible changes in the anisotropy and macrostructure. This is possible due to the optical anisotropy of the elongated polymeric structures in the liquid crystal.[69] FH_1 in Figure 4.11a has an

orientation parallel to the printing direction, which is in agreement with the scanning SAXS experiments shown in Figure 4.10a-c. A filament with low retardance (Figure 4.11b) is obtained, which later increases. The evolution of the macroscopic orientation shows formation of microdomains, starting with a few microdomains and extending to the whole analysed area. The stress induced in the material during extrusion may be the cause of the loss of orientation as a stress release process.[70] PH_I in Figure 4.11c-d, produced a filament oriented in the printing direction with high anisotropy. The retardance later decrease, presumably by the effect of solvent evaporation and relaxation forces. A few minutes after printing, a new region appears in the outer layer of the filament. From this point on the retardance values decay up to a minimum and the intensity of the birefringence signal is too low to consider the measured angle of the optical fast axis to be reliable. That new appearing structure has a similar birefringence signal to the one observed in the lamellar structure PL_α (Figure 4.11d-e) with a very low retardance and homogeneous orientation.

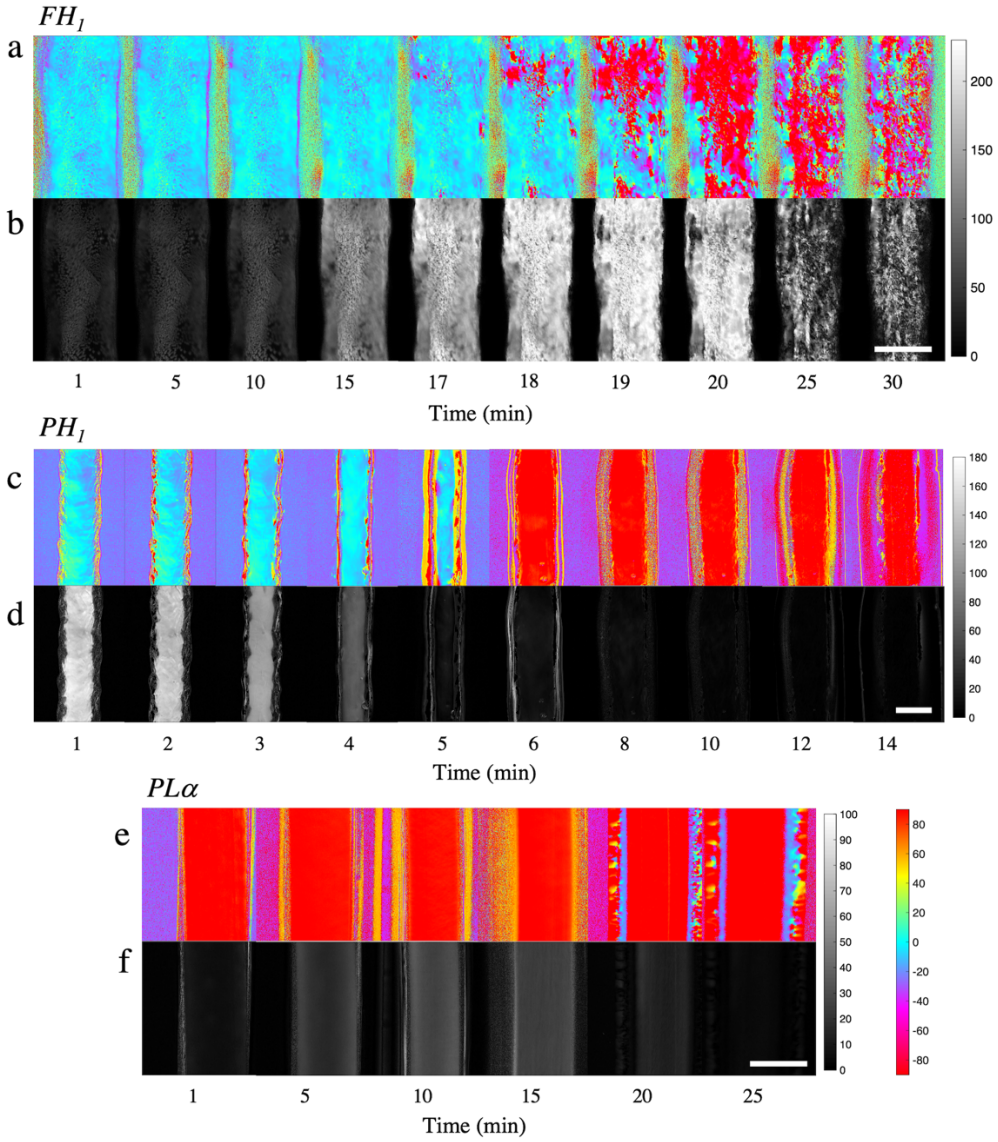

Figure 4.11. Birefringence microscopy of the evolution of the 3D printed liquid crystals over time. The angle of the optical fast axis and retardance are plotted for each material. The most relevant time points were selected to visualize the evolution. The scale bars represent 400 μm.

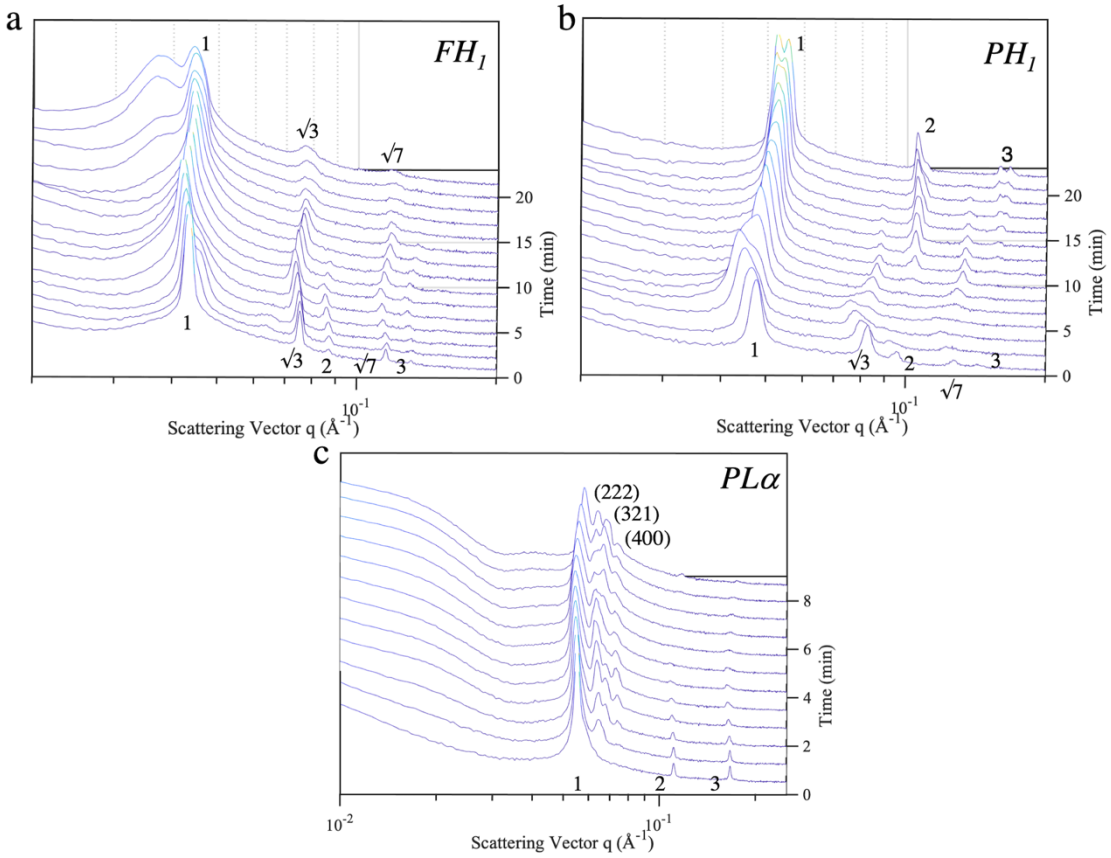

Figure 4.12. Time evolution in the radial integration of the 3D printed lyotropic liquid crystals FH_1 (a), PH_1 (b) and PL_α (c). The scattering vector is represented in the x-axis, time in the y-axis and the intensity of the scattering signal in the z-axis.

The evolution of the 3D printed filaments was also tracked with SAXS by scanning a single line of the filament over time. For FH_1 in Figure 4.12a the initial peak ratio is 1:√3:2:√7, which as commented before, is representative of a hexagonal self-assembled structure. The peaks get broader and less pronounced over time, with the addition of a second population at lower q-values with a broader peak at a characteristic distance of 167.41 Å. This finding could be related with the disordered regions in the multidomain structure observed in Figure 4.11a. The time evolution of PH_1 (Figure 4.12b) starts with the characteristic hexagonal peak ratio 1:√3:2√7 which is transformed into the new ratio 1:2:3 from a lamellar phase. Since the experiment was performed in atmospheric conditions, we assume a change of composition due to the loss of solvent by evaporation, which results in a shift in the phase diagram.[37] This finding supports the results in Figure 4.11c, where the hexagonal structure revealed an abrupt change in the birefringence signal matching the signal obtained in the lamellar phase in Figure 4.11e. The evolution of PL_α in Figure 4.12c shows the initial lamellar peak ratio 1:2:3. The effect of the solvent evaporation produces a new set of three peaks at low q-values, which match a cubic BCC structure, corresponding to the planes (222), (321) and (400),[71,72] Together with the new peaks, a shoulder at low q appears. A fitting with the software SAS View is in agreement with a form factor from a sphere in cubic arrangement with a radius of 136 Å. This estimation is consistent with previous references and with the theoretical sphere radius of the

indexed BCC cubic structure of 148 Å. This result suggests the coexistence of two phases, L_α and I_1. The performed experiments involving extrusion and quick environmental changes are far from the thermodynamic stability, which open the possibility for these processes to occur.

Chapter 5

Conclusions and Outlook

The experiments and results presented in this thesis were centred around the study of the induced anisotropy of lyotropic liquid crystals and techniques to understand their behaviour using imaging methods. Paper I focused on the effect that confined flow has on the nanostructure of the self-assembled liquid crystals. Combining scanning SAXS and microfluidic channels with a controlled flow, the anisotropy and morphological evolution could be visualised with high spatial resolution. The extensional flow introduced by the contractions in the microchannel was expected to be the major source of anisotropy, however this study demonstrated that the shear rate has a strong effect on the liquid crystals. The alignment in the flow direction was caused by the high shear rate in the proximities of the channel walls. The strong effect of shear does not only influence the alignment of the self-assembled cylinders or bilayers, but it is also related with changes in their morphology at a larger scale. The combination of rheology and scanning SAXS revealed a transition from extended lamellae to multilamellar vesicles and the further break-up due to high mechanical stress back into extended structures.

Paper II presented the evolution of the aligned structure of liquid crystals after the confinement in a 3D printer nozzle by *in situ* measurements. The nanostructure of the filament was oriented in the printing direction. An increased and more homogeneous orientation was achieved using larger nozzles diameters. The orientation parameter showed a core-shell structure with a higher oriented outer layer in the less oriented core. The time evolution of the self-assembled structure was studied by SAXS and birefringence imaging. A general trend towards relaxation and disorder was observed at long exposure times to atmospheric condition. The effect of solvent evaporation showed phase transitions to different self-assembled structures as well as co-existence of multiple phases.

A particularly interesting aspect for further studies is a more in-depth analysis of the effect that pure shear and pure extensional flow has on the anisotropy of the examined liquid crystals. Devices based on the microfluidic principles such as the Fluidic Four Roll Mill[73] can reproduce any arbitrary 2D flow-fields, which includes pure shear or pure extensional flows. Combining this technique with scanning SAXS, the anisotropy and nanostructure of the used liquid crystals could be studied applying several flow types. However, the high viscosity of the material makes it challenging to use. The limit of the device is reached with respect to the maximum flow rate and the maximum internal pressure the device resists. In addition, a detailed rheological study of the effect of relaxation forces in the liquid crystals after shear could improve the understanding of the presented lack of uniformity in the printed filament in Paper II. The effects seen in the distribution of angles of orientation might be correlated

with the relaxation time and viscoelasticity of the liquid crystals; however, these processes are not yet fully understood.

Regarding the initial motivation of improving the quality of the bone-mimetic composites, the results showed that the nozzle used for printing will have a critical impact in the final alignment of the composite. It is also important to consider that the shape and dimension of the nozzle to produce ideal alignment will highly depend on the material used. Since the mineralization process takes place in the aqueous domains between the micellar cylinders, the lack of control in the alignment will results in a composite with a lower than expected anisotropy. A poor control in the orientation will therefore influence the mechanical properties of the composite, which is one of the targets in its design. This is also related with the morphological changes seen in the microfluidic experiments. No alignment may be achieved in the case of a lamellar phase formed by multilamellar vesicles. The possibility of a phase change is another important parameter that could eventually influence the final mechanical properties, which means that the environmental conditions and timing of stabilization e.g. cross-linking has to be well controlled. The mineralization process could be affected by a change between the inter-cylinder 1D environment in the hexagonal self-assembled phase and the 2D space between bilayers in the lamellar structure. Thus, the presented work is potentially useful for a more accurate design of the processing parameters in the bone-mimetic composites.

Acknowledgements

I would like to thank the Area of Advance Material Science at Chalmers University of Technology and the Swedish Research Council for providing the funding necessary to develop this work. I would also like to acknowledge the European Union's Horizon 2020 research and innovation programme (EUSMI) for providing funding for some of the synchrotron experiment, and Kristina Stenborgs Stiftelse and the Wallenberg Wood Science Centre (WWSC) for the financial support of the birefringence microscope. I acknowledge the Paul Scherrer Institute, Villigen, Switzerland for the provision of synchrotron radiation beamtime at the beamline cSAXS of the SLS.

A big thanks to my supervisor Marianne Liebi, who put her trust in me. All the knowledge gained in those past years is unmeasurable. You always offer me opportunities to explore, learn and develop to become an independent researcher. I will always be grateful for that.

To my co-supervisor Martin Andersson for all the help I got in the lab and the interesting discussions and to Aleksandar Matic as examiner for taking care of us and everything around.

A huge thanks to everyone in the Division of Materials Physics, current and former members. Thank you for all the great time we spent together, after-works, dinners and for taking me under your wing when I was a newcomer. Despite the times we have now, the environment in the division makes it worth to work here.

I would also like to acknowledge all the help and support I received from the external collaborators at ETH Zurich, the Paul Scherer Institute and Chalmers, especially in the very beginning. You showed me that everyone gets failed experiments and stressful beamtimes, but there is always a chance to learn from them.

Finally, I would like to thank my family who supported me when I decided to leave my country to pursue a new goal. To my friends back in Madrid, that I always keep in mind and love to see every now and then, and to all the new friends I made here in Göteborg that make my life much easier and entertained.

Bibliography

1. Wegst, U. G. K.; Bai, H.; Saiz, E.; Tomsia, A. P.; Ritchie, R. O., Bioinspired structural materials. *Nature Materials* **2015,** *14* (1), 23-36.

2. Yousefi, A.-M.; Hoque, M. E.; Prasad, R. G. S. V.; Uth, N., Current strategies in multiphasic scaffold design for osteochondral tissue engineering: A review. *J Biomed Mater Res A* **2015,** *103* (7), 2460-2481.

3. Stasiak, J.; Brubert, J.; Serrani, M.; Nair, S.; de Gaetano, F.; Costantino, M. L.; Moggridge, G. D., A bio-inspired microstructure induced by slow injection moulding of cylindrical block copolymers. *Soft Matter* **2014,** *10* (32), 6077-6086.

4. He, W.-X.; Rajasekharan, A. K.; Tehrani-Bagha, A. R.; Andersson, M., Mesoscopically Ordered Bone-Mimetic Nanocomposites. *Advanced Materials* **2015,** *27* (13), 2260-2264.

5. Kroto, H. W.; Heath, J. R.; O'Brien, S. C.; Curl, R. F.; Smalley, R. E., C60: Buckminsterfullerene. *Nature* **1985,** *318* (6042), 162-163.

6. Iijima, S., Helical microtubules of graphitic carbon. *Nature* **1991,** *354* (6348), 56-58.

7. Eigler, D. M.; Schweizer, E. K., Positioning single atoms with a scanning tunnelling microscope. *Nature* **1990,** *344* (6266), 524-526.

8. Zeng, S.; Yong, K.-T.; Roy, I.; Dinh, X.-Q.; Yu, X.; Luan, F., A Review on Functionalized Gold Nanoparticles for Biosensing Applications. *Plasmonics* **2011,** *6* (3), 491.

9. Jariwala, D.; Sangwan, V. K.; Lauhon, L. J.; Marks, T. J.; Hersam, M. C., Carbon nanomaterials for electronics, optoelectronics, photovoltaics, and sensing. *Chemical Society Reviews* **2013,** *42* (7), 2824-2860.

10. Teleanu, D. M.; Chircov, C.; Grumezescu, A. M.; Volceanov, A.; Teleanu, R. I., Contrast Agents Delivery: An Up-to-Date Review of Nanodiagnostics in Neuroimaging. *Nanomaterials* **2019,** *9* (4).

11. Song, W.; Musetti, S. N.; Huang, L., Nanomaterials for cancer immunotherapy. *Biomaterials* **2017,** *148*, 16-30.

12. Giacomelli, C.; Borsali, R., Disordered Phase and Self-Organization of Block Copolymer Systems. In *Soft Matter Characterization*, Borsali, R.; Pecora, R., Eds. Springer Netherlands: Dordrecht, 2008; pp 133-189.

13. Jones, R. A. L.; Jones, R. A. L.; R Jones, P., *Soft Condensed Matter*. OUP Oxford: Great Britain, 2002; p 195.

14. Israelachvili, J. N., Thermodynamic Principles of Self-Assembly. In *Intermolecular and Surface Forces (Third Edition)*, Israelachvili, J. N., Ed. Academic Press: San Diego, 2011; pp 503-534.

15. Tanford, C., Thermodynamics of Micelle Formation: Prediction of Micelle Size and Size Distribution. *Proceedings of the National Academy of Sciences* **1974,** *71* (5), 1811.

16. Bates, F. S.; Fredrickson, G. H., Block Copolymer Thermodynamics: Theory and Experiment. *Annual Review of Physical Chemistry* **1990,** *41* (1), 525-557.

17. Imran, M.; Shah, M. R.; Shafiullah, Chapter 10 - Amphiphilic block copolymers–based micelles for drug delivery. In *Design and Development of New Nanocarriers*, Grumezescu, A. M., Ed. William Andrew Publishing: 2018; pp 365-400.

18. Feng, H.; Lu, X.; Wang, W.; Kang, N.-G.; Mays, J. W., Block Copolymers: Synthesis, Self-Assembly, and Applications. *Polymers-Basel* **2017,** *9* (10).

19. Kim, J. H.; Jin, H. M.; Yang, G. G.; Han, K. H.; Yun, T.; Shin, J. Y.; Jeong, S.-J.; Kim, S. O., Smart Nanostructured Materials based on Self-Assembly of Block Copolymers. *Adv Funct Mater* **2020,** *30* (2), 1902049.

20. Lim, S.-H.; Lee, T.; Oh, Y.; Narayanan, T.; Sung, B. J.; Choi, S.-M., Hierarchically self-assembled hexagonal honeycomb and kagome superlattices of binary 1D colloids. *Nature Communications* **2017,** *8* (1), 360.

21. Ha, J.-M.; Lim, S.-H.; Dey, J.; Lee, S.-J.; Lee, M.-J.; Kang, S.-H.; Jin, K. S.; Choi, S.-M., Micelle-Assisted Formation of Nanoparticle Superlattices and Thermally Reversible Symmetry Transitions. *Nano Letters* **2019,** *19* (4), 2313-2321.

22. Allen, S. M.; Thomas, E. L., Liquid-Crystalline State. In *The Structure of Materials*, Wiley: 1999; pp 213-248.

23. Li, L.-s.; Walda, J.; Manna, L.; Alivisatos, A. P., Semiconductor Nanorod Liquid Crystals. *Nano Letters* **2002,** *2* (6), 557-560.

24. Pomerantz, W. C.; Yuwono, V. M.; Pizzey, C. L.; Hartgerink, J. D.; Abbott, N. L.; Gellman, S. H., Nanofibers and Lyotropic Liquid Crystals from a Class of Self-Assembling β-Peptides. *Angewandte Chemie International Edition* **2008,** *47* (7), 1241-1244.

25. Baruchel, J.; Hodeau, J. L.; Lehmann, M. S.; Regnard, J. R.; Schlenker, C., Structure of Liquid Crystals. In *Neutron and Synchrotron Radiation for Condensed Matter Studies: Applications to Soft Condensed Matter and Biology*, Springer-Verlag: Berlin, 1994; Vol. 3, p 332.

26. Schwieger, W.; Machoke, A. G.; Weissenberger, T.; Inayat, A.; Selvam, T.; Klumpp, M.; Inayat, A., Hierarchy concepts: classification and preparation strategies for zeolite containing materials with hierarchical porosity. *Chemical Society Reviews* **2016,** *45* (12), 3353-3376.

27. Fratzl, P.; Weinkamer, R., Nature's hierarchical materials. *Progress in Materials Science* **2007,** *52* (8), 1263-1334.

28. Brodoceanu, D.; Bauer, C. T.; Kroner, E.; Arzt, E.; Kraus, T., Hierarchical bioinspired adhesive surfaces—a review. *Bioinspiration & Biomimetics* **2016,** *11* (5), 051001.

29. Gao, H.; Wang, X.; Yao, H.; Gorb, S.; Arzt, E., Mechanics of hierarchical adhesion structures of geckos. *Mechanics of Materials* **2005,** *37* (2), 275-285.

30. Northen, M. T.; Greiner, C.; Arzt, E.; Turner, K. L., A Gecko-Inspired Reversible Adhesive. *Advanced Materials* **2008,** *20* (20), 3905-3909.

31. Jeong, H. E.; Lee, J.-K.; Kim, H. N.; Moon, S. H.; Suh, K. Y., A nontransferring dry adhesive with hierarchical polymer nanohairs. *Proceedings of the National Academy of Sciences* **2009,** *106* (14), 5639.

32. Liu, Y.; Luo, D.; Wang, T., Hierarchical Structures of Bone and Bioinspired Bone Tissue Engineering. *Small* **2016,** *12* (34), 4611-4632.

33. Truby, R. L.; Lewis, J. A., Printing soft matter in three dimensions. *Nature* **2016,** *540* (7633), 371-378.

34. Patel, B. B.; Walsh, D. J.; Kim, D. H.; Kwok, J.; Lee, B.; Guironnet, D.; Diao, Y., Tunable structural color of bottlebrush block copolymers through direct-write 3D printing from solution. *Science Advances* **2020,** *6* (24), eaaz7202.

35. Rajasekharan, A. K.; Lotsari, A.; Lutz-Bueno, V.; Liebi, M.; Andersson, M., Bioinspired Structural Hierarchy within Macroscopic Volumes of Synthetic Composites. *Advanced Healthcare Materials* **2018,** *7* (18).

36. Georgiadis, M.; Müller, R.; Schneider, P., Techniques to assess bone ultrastructure organization: orientation and arrangement of mineralized collagen fibrils. *Journal of The Royal Society Interface* **2016,** *13* (119), 20160088.

37. Holmqvist, P.; Alexandridis, P.; Lindman, B., Modification of the Microstructure in Block Copolymer−Water−"Oil" Systems by Varying the Copolymer Composition and the "Oil" Type: Small-Angle X-ray Scattering and Deuterium-NMR Investigation. *The Journal of Physical Chemistry B* **1998,** *102* (7), 1149-1158.

38. Holmqvist, P.; Alexandridis, P.; Lindman, B., Phase Behavior and Structure of Ternary Amphiphilic Block Copolymer−Alkanol−Water Systems: Comparison of Poly(ethylene oxide)/Poly(propylene oxide) to Poly(ethylene oxide)/Poly(tetrahydrofuran) Copolymers. *Langmuir* **1997,** *13* (9), 2471-2479.

39. Holmqvist, P.; Alexandridis, P.; Lindman, B., Modification of the Microstructure in Poloxamer Block Copolymer−Water−"Oil" Systems by Varying the "Oil" Type. *Macromolecules* **1997,** *30* (22), 6788-6797.

40. Ivanova, R.; Lindman, B.; Alexandridis, P., Evolution in Structural Polymorphism of Pluronic F127 Poly(ethylene oxide)−Poly(propylene oxide) Block Copolymer in Ternary Systems with Water and Pharmaceutically Acceptable Organic Solvents: From "Glycols" to "Oils". *Langmuir* **2000,** *16* (23), 9058-9069.

41. Alexandridis, P.; Olsson, U.; Lindman, B., Self-Assembly of Amphiphilic Block Copolymers: The (EO)13(PO)30(EO)13-Water-p-Xylene System. *Macromolecules* **1995,** *28* (23), 7700-7710.

42. Lutz-Bueno, V.; Zhao, J.; Mezzenga, R.; Pfohl, T.; Fischer, P.; Liebi, M., Scanning-SAXS of microfluidic flows: nanostructural mapping of soft matter. *Lab on a Chip* **2016,** *16* (20), 4028-4035.

43. Schnablegger, H.; Singh, Y., The SAXS guide: getting acquainted with the principles. *Austria: Anton Paar GmbH* **2011**, 1-124.

44. Liebi, M.; Kohlbrecher, J.; Ishikawa, T.; Fischer, P.; Walde, P.; Windhab, E. J., Cholesterol Increases the Magnetic Aligning of Bicellar Disks from an Aqueous Mixture of DMPC and DMPE–DTPA with Complexed Thulium Ions. *Langmuir* **2012,** *28* (29), 10905-10915.

45. Bunk, O.; Bech, M.; Jensen, T. H.; Feidenhans'l, R.; Binderup, T.; Menzel, A.; Pfeiffer, F., Multimodal x-ray scatter imaging. *New Journal of Physics* **2009,** *11* (12).

46. van Gurp, M., The use of rotation matrices in the mathematical description of molecular orientations in polymers. *Colloid and Polymer Science* **1995,** *273* (7), 607-625.

47. Yu, J.; Tian, F.; Chen, S.; Wang, X.; Zhang, Y.; Wang, H., Structure and property development of aromatic copolysulfonamide fibers during wet spinning process. *Journal of Applied Polymer Science* **2015,** *132* (31).

48. Kraft, P.; Bergamaschi, A.; Broennimann, C.; Dinapoli, R.; Eikenberry, E. F.; Henrich, B.; Johnson, I.; Mozzanica, A.; Schleputz, C. M.; Willmott, P. R.; Schmitt, B., Performance of single-photon-counting PILATUS detector modules. *J Synchrotron Radiat* **2009,** *16* (Pt 3), 368-75.

49. Barnes, H. A.; Hutton, J. F.; Walters, K., An Introduction to Rheology. In *An Introduction to Rheology*, Walters, K., Ed. Elsevier: 1989; Vol. 3.

50. Malvern-Instruments, *A Basic Introduction to Rheology*. 2016.

51. Haward, S. J.; Toda-Peters, K.; Shen, A. Q., Steady viscoelastic flow around high-aspect-ratio, low-blockage-ratio microfluidic cylinders. *Journal of Non-Newtonian Fluid Mechanics* **2018,** *254*, 23-35.

52. Cardiel, J. J.; Furusho, H.; Skoglund, U.; Shen, A. Q., Formation of crystal-like structures and branched networks from nonionic spherical micelles. *Scientific Reports* **2015,** *5* (1), 17941.

53. Cardiel, J. J.; Zhao, Y.; De La Iglesia, P.; Pozzo, L. D.; Shen, A. Q., Turning up the heat on wormlike micelles with a hydrotopic salt in microfluidics. *Soft Matter* **2014,** *10* (46), 9300-9312.

54. Shane, N.; John, F.; Oriol, A.; Bart, K. In *Imaging with photoelastic modulators*, Proc.SPIE, 2014.

55. Han, C.-Y.; Chao, Y.-F., Photoelastic modulated imaging ellipsometry by stroboscopic illumination technique. *Rev Sci Instrum* **2006,** *77* (2), 023107.

56. Winey, K. I.; Patel, S. S.; Larson, R. G.; Watanabe, H., Interdependence of shear deformations and block copolymer morphology. *Macromolecules* **1993,** *26* (10), 2542-2549.

57. Winter, H. H.; Chambon, F., Analysis of Linear Viscoelasticity of a Crosslinking Polymer at the Gel Point. *J Rheol* **1986,** *30* (2), 367-382.

58. Kádár, R.; Fazilati, M.; Nypelö, T., Unexpected microphase transitions in flow towards nematic order of cellulose nanocrystals. *Cellulose* **2020,** *27* (4), 2003-2014.

59. Hyun, K.; Wilhelm, M.; Klein, C. O.; Cho, K. S.; Nam, J. G.; Ahn, K. H.; Lee, S. J.; Ewoldt, R. H.; McKinley, G. H., A review of nonlinear oscillatory shear tests: Analysis and application of large amplitude oscillatory shear (LAOS). *Progress in Polymer Science* **2011,** *36* (12), 1697-1753.

60. Hyun, K.; Nam, J. G.; Wilhellm, M.; Ahn, K. H.; Lee, S. J., Large amplitude oscillatory shear behavior of PEO-PPO-PEO triblock copolymer solutions. *Rheol Acta* **2006,** *45* (3), 239-249.

61. Richtering, W. In *Investigation of shear-induced structures in lyotropic mesophases by scattering experiments*, Optical Methods and Physics of Colloidal Dispersions, Darmstadt, 1997//; Palberg, T.; Ballauff, M., Eds. Steinkopff: Darmstadt, 1997; pp 90-96.

62. Hyun, K.; Kim, S. H.; Ahn, K. H.; Lee, S. J., Large amplitude oscillatory shear as a way to classify the complex fluids. *Journal of Non-Newtonian Fluid Mechanics* **2002,** *107* (1), 51-65.

63. Li, X.; Park, E.-k.; Hyun, K.; Oktavia, L.; Kwak, M., Rheological analysis of core-stabilized Pluronic F127 by semi-interpenetrating network (sIPN) in aqueous solution. *J Rheol* **2017,** *62* (1), 107-120.

64. Trebbin, M.; Steinhauser, D.; Perlich, J.; Buffet, A.; Roth, S. V.; Zimmermann, W.; Thiele, J.; Förster, S., Anisotropic particles align perpendicular to the flow direction in narrow microchannels. *Proceedings of the National Academy of Sciences* **2013,** *110* (17), 6706.

65. Son, Y., Determination of shear viscosity and shear rate from pressure drop and flow rate relationship in a rectangular channel. *Polymer* **2007,** *48* (2), 632-637.

66. Martin, H. P.; Brooks, N. J.; Seddon, J. M.; Luckham, P. F.; Terrill, N. J.; Kowalski, A. J.; Cabral, J. T., Microfluidic processing of concentrated surfactant mixtures: online SAXS, microscopy and rheology. *Soft Matter* **2016,** *12* (6), 1750-1758.

67. Diat, O.; Roux, D.; Nallet, F., Effect of shear on a lyotropic lamellar phase. *J. Phys. II France* **1993,** *3* (9), 1427-1452.

68. Lewis, J. A., Direct Ink Writing of 3D Functional Materials. *Adv Funct Mater* **2006,** *16* (17), 2193-2204.

69. Cardiel, J. J.; Takagi, D.; Tsai, H.-F.; Shen, A. Q., Formation and flow behavior of micellar membranes in a T-shaped microchannel. *Soft Matter* **2016,** *12* (39), 8226-8234.

70. Emmermacher, J.; Spura, D.; Cziommer, J.; Kilian, D.; Wollborn, T.; Fritsching, U.; Steingroewer, J.; Walther, T.; Gelinsky, M.; Lode, A., Engineering considerations on extrusion-based bioprinting: interactions of material behavior, mechanical forces and cells in the printing needle. *Biofabrication* **2020,** *12* (2), 025022.

71. Svensson, B.; Alexandridis, P.; Olsson, U., Self-Assembly of a Poly(ethylene oxide)/Poly(propylene oxide) Block Copolymer (Pluronic P104, (EO)27(PO)61(EO)27) in the Presence of Water and Xylene. *The Journal of Physical Chemistry B* **1998,** *102* (39), 7541-7548.

72. Ivanova, R.; Lindman, B.; Alexandridis, P., Effect of Glycols on the Self-Assembly of Amphiphilic Block Copolymers in Water. 1. Phase Diagrams and Structure Identification. *Langmuir* **2000,** *16* (8), 3660-3675.

73. Lee, J. S.; Dylla-Spears, R.; Teclemariam, N. P.; Muller, S. J., Microfluidic four-roll mill for all flow types. *Applied Physics Letters* **2007,** *90* (7), 074103.